



Absorption Spectra of Electrified Hydrogen Molecules

Mark A. Walker Manly Astrophysics, 15/41-42 East Esplanade, Manly, NSW 2095, Australia; mark.walker@manlyastrophysics.org

Received 2021 July 29; revised 2022 March 31; accepted 2022 April 1; published 2022 June 8

Abstract

Molecular hydrogen normally has only weak, quadrupole transitions between its rovibrational states, but in a static electric field it acquires a dipole moment and a set of allowed transitions. Here we use published ab initio calculations of the static electrical response tensors of the H_2 molecule to construct the perturbed rovibrational eigensystem and its ground state absorptions. We restrict attention to two simple field configurations that are relevant to condensed hydrogen molecules in the interstellar medium (ISM): a uniform electric field and the field of a pointlike charge. The energy eigenstates are mixtures of vibrational and angular momentum eigenstates so there are many transitions that satisfy the dipole selection rules. We find that mixing is strongest among the states with high vibrational excitation, leading to hundreds of absorption lines across the optical and near-infrared. These spectra are very different from that of the field-free molecule, so if they appeared in astronomical data they would be difficult to assign. Furthermore, in a condensed environment the excited states likely have short lifetimes to internal conversion, giving the absorption lines a diffuse appearance. We therefore suggest electrified H_2 as a possible carrier of the diffuse interstellar bands (DIBs). We further argue that in principle it may be possible to account for all of the DIBs with this one carrier. However, despite electrification, the transitions are not very strong and a large column of condensed H_2 would be required, making it difficult to reconcile this possibility with our current understanding of the ISM.

Unified Astronomy Thesaurus concepts: [Molecular physics \(2058\)](#); [Molecular spectroscopy \(2095\)](#); [Interstellar dust \(836\)](#); [Interstellar dust extinction \(837\)](#); [Diffuse interstellar bands \(379\)](#); [Interstellar line absorption \(843\)](#)

Supporting material: machine-readable tables

1. Introduction

It is widely appreciated that cold, dense gas is difficult to see and that this is in part because its main constituents—that is, helium and molecular hydrogen—have no electric dipole transitions below the far-UV. It is therefore possible that galaxies could contain substantial, undetected reservoirs of cold, dense gas, and Pfenninger et al. (1994) argued that must be the case in order to account for the observed properties of star-forming galaxies. Pfenninger & Combes (1994) noted that in such reservoirs the hydrogen ought to be close to its saturation vapor pressure and could manifest particles of solid H_2 —an idea that ultimately led to a revival of interest in solid H_2 as a candidate material for interstellar dust, for the reasons outlined below.

An important aspect of condensed H_2 is that its ionization chemistry differs from that of the gas phase, with the dominant ionization product being H_3^+ for gaseous H_2 (see, e.g., the review by Miller et al. 2020) and the balance shifting toward H_6^+ in condensed environments (e.g., Jaksch et al. 2008). As a result, the H_6^+ molecule—which was only recently revealed in the laboratory, using electron spin resonance (Kumada et al. 2005)—could be abundant in the interstellar medium (ISM). The rovibrational spectra of that molecule offer a means of recognizing solid hydrogen in the ISM but have not yet been studied in the laboratory. Using ab initio calculation, Lin et al. (2011) demonstrated that the two most important isotopomers, namely, H_6^+ and $(HD)_3^+$, both have vibrational transitions that

are coincident with strong mid-infrared lines observed from the ISM and suggested that they could be the carriers of the observed lines.

Considering charged species such as H_6^+ inside a matrix of solid H_2 naturally suggested another interesting possibility (Lin et al. 2011): astrophysical hydrogen ices might be substantially more robust than their laboratory counterparts, as a result of electrostatic interactions associated with ionic impurities. And interstellar ice particles, even if they were initially pure H_2 , would soon acquire charged impurities as a result of bombardment by charged particles and ionizing photons. That is a critical point because it was shown by Field (1969) and Greenberg & de Jong (1969) that pure H_2 ice sublimates rapidly under typical interstellar conditions, and subsequent to those papers solid hydrogen was eschewed as a candidate material for interstellar dust. Consequently, there is a well-developed body of theoretical work on silicate and carbonaceous interstellar dust grains (e.g., Draine 2003), but we know very little about the possible manifestations of H_2 ice particles.

The influence of collisional charging on the lifetime of hydrogen dust particles was considered in detail by Walker (2013), who emphasized the important role played by the unusual electronic properties of solid hydrogen. Specifically, the conduction band lies above the energy of an electron in vacuo, which makes it difficult for electrons to penetrate the lattice; instead they tend to become trapped above the surface, where they form a two-dimensional electron gas (Cole 1970). But there is no such barrier for ionic species, which easily penetrate into the matrix, so that grain charging can create large column densities in charges of both signs and a grain that is close to overall neutrality. Consequently, the electric fields inside the matrix may reach high values, with a correspondingly large

attenuation of the H_2 sublimation rate and a greatly increased lifetime of solid H_2 particles (Walker 2013). In this picture the electric field is not localized and may be considered to be approximately uniform within the solid—as an idealized example one can imagine the case of a plate-like crystal habit (such as is known to occur among the many types of terrestrial H_2O snowflakes, Libbrecht 2017) with positive charges near the midplane and electrons bound to the surfaces.

At the opposite extreme it has long been recognized that localized electric fields can bind H_2 ligands and that this can occur under conditions where pure H_2 would not condense. For example, Sandford & Allamandola (1993) undertook laboratory studies of the condensation of H_2 molecules onto water ice, which is promoted by the electric dipole moment of H_2O , and Duley (1996) analyzed the formation mechanisms of H_2 clusters around ionic species in the context of dense interstellar clouds. If cation and anion clusters are both present then they can be expected to aggregate, leading to dust particles of hydrogen ice. Provided that the identity of the main impurities is known, ices of this type can in principle be recognized by the absorption spectra of the impurity species, whose lines are expected to be slightly shifted in wavelength as a consequence of perturbation by the H_2 ligands—the “matrix shift.” It was suggested by Bernstein et al. (2013) that the matrix-shifted electronic transitions of a large set of impurity species could be responsible for the absorption lines known as the diffuse interstellar bands (DIBs).

An absorption signature of the H_2 matrix itself would be valuable because it would allow the main component of a hydrogen ice particle to be observed directly and because it would obviate the need for a detailed understanding of the impurity content of the ice. It is known that pure solid para- H_2 manifests spectral features that are absent in the gas phase (e.g., Mengel et al. 1998), so such a signature exists, but in practice those spectral features are much too weak to be detectable in astrophysical dust (Kettwich et al. 2015). Indeed, by modeling the refractive index, Kettwich et al. (2015) demonstrated that extinction by particles of pure solid para- H_2 should be scattering dominated at frequencies below the far-UV and that even the strongest rovibrational absorptions (i.e., those that are also present in gas phase) are too weak to be seen in the extinction curve. In turn, this is, of course, because the rovibrational lines of the isolated H_2 molecule are electric quadrupole transitions—with some contribution from magnetic dipole (Rouef et al. 2019)—and are all very weak. However, just as the H_2 grain sublimation rate can be strongly influenced by the presence of electric charges, so can the absorption spectrum of the hydrogen matrix. The key point is that H_2 becomes infrared active in the presence of a static electric field, because the field polarizes the molecule (Condon 1932). An electric field also changes the energy levels of H_2 , lifting degeneracies and causing shifts and splittings in its spectral lines—a condition we refer to as “electrified.” The radiative transitions of electrified molecules can be thought of as the zero-frequency limit of Raman spectra, with corresponding selection rules (Condon 1932).

In this paper we calculate the ortho-/para- H_2 ground state absorption spectra that arise in two simple field configurations: a uniform field and the field of a pointlike charge. These particular choices were motivated by consideration of the types of fields that might plausibly be encountered inside charged dust grains of hydrogen ice, as discussed above. It is clear at the

outset that our adopted field configurations are simplified models of the physical circumstances under consideration because, for example, we are neglecting the field due to the induced dipole moments of neighboring H_2 molecules. Nevertheless the calculated spectra are complex and interesting in their own right, and they provide useful first approximations that establish a foundation for more sophisticated treatments.

There have been numerous experimental studies of the absorption spectra of irradiated solid hydrogens (e.g., Souers et al. 1980; Brooks et al. 1985; Momose et al. 2001), in which new features have been observed and attributed to the Stark-shifted absorptions of H_2 (or D_2 etc.) molecules adjacent to charged impurities. By contrast there has been relatively little exploration of their theoretical counterpart spectra, despite the availability of suitable electrical response tensors (Kofos & Wolniewicz 1967; Poll & Wolniewicz 1978). That is understandable as the strong electric fields that are encountered lead to high levels of mixing among the basis states, and at the time the experimental studies were being pursued the task of diagonalizing the Hamiltonian matrix was computationally challenging. The principal theoretical resource to date has been the work of Poll & Hunt (1985), who quantified the energy levels of 16 low-lying rovibrational states of H_2 , D_2 , and T_2 as a function of the separation between the molecule and a pointlike charge of either sign. In Section 3.3 we give a quantitative comparison between their results, for the case of H_2 , and ours.

There are some qualitative differences between the treatment of Poll & Hunt (1985) and the work presented here. First, because we are concerned with the astrophysical context, we have not attempted to characterize the states of any of the heavier isotopes of hydrogen. Second, our calculations are not restricted to a few of the low-lying eigenstates: all of the perturbed eigenstates are characterized because it is now computationally feasible to do so. Third, we evaluate the electric dipole transition matrix elements between all pairs of rovibrational states, allowing us to determine the transition strength and natural width appropriate to every line in the absorption spectrum of the electrified molecule. Finally, we extend the electrical response model of H_2 from the two second-rank tensors—the permanent quadrupole, Θ , and the dipole polarizability, α —that were considered by Poll & Hunt (1985) to include five response tensors of fourth rank. Our expansion in scope of the electrical response model was made possible by the recent ab initio calculations of Miliordos & Hunt (2018), whose treatment of H_2 is comprehensive up to fourth rank.

The structure of this paper is as follows. In Section 2 we set out the inputs needed for our calculations, namely, the eigenstates of the unperturbed H_2 molecule and the perturbation introduced by a static electric field. Some details of the latter are placed in appendices as they are required for calculations but not essential for understanding. Section 3 describes the eigenstates of the perturbed molecule, which we obtain by diagonalizing the perturbed Hamiltonian for three distinct cases: a uniform electric field, a pointlike elementary positive charge, and a pointlike elementary negative charge. In each case the eigensystem is a function of a single parameter (e.g., field strength). Section 4 presents our calculated absorption spectra of ground state molecules for each of these cases; both ortho- and para- sequences are treated, so there are two ground states and two absorption spectra for every field

configuration. Section 5 considers how our calculated spectra might relate to the observed properties of the ISM, with particular emphasis on the possibility that electrified H_2 might be a carrier of the DIBs. In Section 6 we detail various issues arising with that idea, one of which is of particular importance because it is a potential showstopper: the strength of the transitions of electrified H_2 . The problem, discussed in Section 6.4, is that trace quantities of electrified H_2 cannot explain the DIBs—a substantial fraction of the total interstellar mass would need to be in the form of condensed hydrogen, implying substantial revisions to our understanding of the ISM. Section 6 also provides some commentary on the limitations of the theoretical framework that we have employed. Summary and conclusions follow in Section 7.

2. Description of the Unperturbed Molecule

In the present paper we will be concerned exclusively with the electronic ground state, $X^1\Sigma_g^+$, of the H_2 molecule, and although that restriction will not be restated from here onward, it should be understood to apply throughout.

The H_2 molecule has been well studied both experimentally and theoretically. It is known that there are 302 bound rovibrational levels of H_2 (Komasa et al. 2011), characterized by two quantum numbers: vibrational, v , with $0 \leq v \leq 14$; and total angular momentum, j , with $0 \leq j \leq 31$. Each level is a multiplet of $2j + 1$ degenerate states distinguished from each other by one component of the angular momentum—which we take to be the z component—and labeled with the corresponding quantum number, m , where $-j \leq m \leq j$. The total number of bound rovibrational states $|v, j, m\rangle$ is thus 7086; this set of states constitutes the basis that spans our modeling space. Unfortunately, there is no guarantee that this basis suffices to describe the bound states of the perturbed molecule—in general the unbound continuum states may also be required—and in Section 4.2.3 we draw attention to evidence for incompleteness in the case of strong electric fields.

Theoretical level energies are known to high precision and compare favorably with the available laboratory spectroscopy, with estimated accuracy better than 0.001 cm^{-1} (Komasa et al. 2019). Although the level energy calculations themselves are naturally done in atomic units, it is conventional in laboratory spectroscopy to use the wavenumber $1/\lambda$, where λ is the vacuum wavelength of the transition in centimeters; we follow that convention throughout this paper.

The level energies are, of course, just the eigenvalues of the rovibrational Hamiltonian matrix, so adopting the $|v, j, m\rangle$ states as our basis, and using the energy eigenvalues reported by Komasa et al. (2011), we can immediately construct the unperturbed Hamiltonian as a diagonal matrix whose entries are those eigenvalues. In principle that construction could include all the rovibrational states of H_2 , but in practice it is better to split the calculation in two, considering ortho- H_2 ($j = 1, 3, 5, \dots$) and para- H_2 ($j = 0, 2, 4, \dots$) separately. As is well known, these two sequences can usually be considered as distinct species because the ortho- states all have parallel nuclear spins (nuclear spin triplet), while the para- states all have antiparallel spins (nuclear spin singlet) and the rate of interconversion is very small (Freiman & Crespo 2017). We will see that the perturbations introduced by a static electric field do not mix ortho- states with para- states, so it is valid to consider the two sequences separately. Doing so has computational advantages because it is quicker to construct and

diagonalize the two separate Hamiltonians than it is to handle everything in a single matrix.

2.1. Unperturbed States

To determine the energy eigenstates of the perturbed molecule we need to calculate the Hamiltonian matrix elements of the perturbation, and in order to evaluate those elements we must first characterize the unperturbed states themselves. In other words, we must solve the time-independent Schrödinger equation for the unperturbed molecule. To do so we employ the Born–Oppenheimer approximation and consider only the wave function describing the internuclear separation r . As usual we can separate the angular and radial variables, leading to eigenfunctions of the form $\psi(r, \theta, \phi) = Y_{j,m}(\theta, \phi)\chi_{v,j}(r)$, in terms of the spherical harmonics $Y_{j,m}$. The remaining differential equation describes the dependence of the wave functions on the radial coordinate:

$$\frac{d}{dr} \left(r^2 \frac{d\chi_{v,j}}{dr} \right) + \frac{m_p}{m_e} r^2 \times [E_{v,j} - V] \chi_{v,j} - j(j+1)\chi_{v,j} = 0, \quad (1)$$

with all quantities in atomic units. To solve for the various $\chi_{v,j}$ and the corresponding energy eigenvalues $E_{v,j}$ it is necessary to know the internuclear potential $V(r)$; we use the Born–Oppenheimer potential tabulated by Pachucki (2010) plus the adiabatic correction function given by Pachucki & Komasa (2014).

To obtain solutions to Equation (1) we use the Numerov–Cooley method (Cooley 1961; Johnson 1977), which is sixth-order accurate in the step size, to solve for the function $\mathcal{R}_{v,j} \equiv r \chi_{v,j}$. Our wave functions were determined on a uniform grid of 20,000 points extending to $r = 20$ (atomic units).¹ As part of the solution process we obtain our own set of eigenvalues. Our eigenvalues differ by $2 \pm 2 \text{ cm}^{-1}$ from the much more accurate eigenvalues of Komasa et al. (2011), implying systematic errors at the level $\sim 10^{-4}$ (fractional error in the eigenvalue) for most of the eigenstates. This level of accuracy suffices for constructing the matrix elements of the electrical perturbation because it is substantially smaller than the systematic errors in the input values of the electrical response tensors (see next section). We note, however, that the level $(v, j) = (14, 4)$ has such a small binding energy (0.0265 cm^{-1} , Komasa et al. 2011) that it cannot be adequately described by our approach and we have therefore excluded it from our calculations. That leaves us with 155 energy levels and 3567 possible states for para- H_2 and 146 energy levels and 3510 states for ortho- H_2 .

2.2. Static Electrical Response of H_2

Recent ab initio calculations by Miliordos & Hunt (2018) have substantially improved the characterization of the electrical response of the H_2 molecule. In addition to the second-rank response tensors—the permanent quadrupole moment, Θ , and the dipole polarizability, α —Miliordos & Hunt (2018) evaluated the permanent hexadecapole moment, Φ , the quadrupole polarizability, C , the dipole–octupole polarizability, E , the dipole–dipole–quadrupole hyperpolarizability, B , and the second

¹ The atomic unit of distance is also known as the Bohr radius; the approximate numerical value is 0.529 \AA .

dipole hyperpolarizability, γ . In other words, all of the (nonzero) response tensors up to fourth rank. And each independent component of those tensors was tabulated by Miliordos & Hunt (2018) over a wide enough range of internuclear separations ($0.567 \leq r \leq 10$, atomic units) that accurate matrix elements can be evaluated between all pairs of bound rovibrational states.

Good numerical accuracy was demonstrated by Miliordos & Hunt (2018), with test calculations for the case of a ground state hydrogen atom yielding electrical response tensors that differ from the known (exact) values by only $\sim 0.4\%$. Although that is a small error, it is large compared with the systematic errors in the eigenfunctions we have constructed (Section 2.1), so we do not expect the latter to limit the accuracy of the matrix elements we have evaluated.

Because of the symmetries of the H_2 molecule (point group $D_{\infty h}$), only 16 independent components are required to fully describe the seven response tensors under consideration (Buckingham 1967; McLean & Yoshimine 1967; Miliordos & Hunt 2018). For the convenience of readers, the behavior of those components as a function of internuclear separation is presented in Appendix A; they are specified in a Cartesian coordinate system (X, Y, Z) in which the Z -axis is aligned with the internuclear separation vector. The response tensors in the laboratory coordinate system, (x, y, z), depend also on the orientation of the internuclear axis and can be related to those in the molecular basis using the expressions given by Buckingham (1967), for Θ , α , C , B , and γ and by Bohr & Hunt (1987) for Φ and E . We are thus in a position to evaluate the perturbation of the energy of the molecule (Miliordos & Hunt 2018)

$$\begin{aligned} \Delta E = & -\frac{1}{3}\Theta_{\alpha\beta}F'_{\alpha\beta} - \frac{1}{105}\Phi_{\alpha\beta\gamma\delta}F'''_{\alpha\beta\gamma\delta} - \frac{1}{2}\alpha_{\alpha\beta}F_{\alpha}F_{\beta} \\ & - \frac{1}{6}C_{\alpha\beta,\gamma\delta}F'_{\alpha\beta}F'_{\gamma\delta} - \frac{1}{15}E_{\alpha,\beta\gamma\delta}F_{\alpha}F''_{\beta\gamma\delta} \\ & - \frac{1}{6}B_{\alpha,\beta,\gamma\delta}F_{\alpha}F_{\beta}F'_{\gamma\delta} - \frac{1}{24}\gamma_{\alpha\beta\gamma\delta}F_{\alpha}F_{\beta}F_{\gamma}F_{\delta}, \end{aligned} \quad (2)$$

arising from the imposed electric field, F , and its first three gradients $F' \equiv \nabla F$, and so on.

3. Electrified States of Molecular Hydrogen

To determine the eigenstates of H_2 in the presence of an electric field, we first evaluate the Hamiltonian matrix elements of the electrical perturbation in the unperturbed basis. Those elements are then added to the unperturbed Hamiltonian, which is diagonal and very accurately known, and the full Hamiltonian is diagonalized to yield the new eigenvalues and eigenvectors.

The Cartesian form of the perturbation given in Equation (2) is not well suited to the task of rapid calculation of the millions of elements that make up the Hamiltonian matrix. For that purpose it is much more convenient to expand the perturbation in spherical harmonics. For the electric field configurations under consideration in this paper, both of which are axisymmetric, the only nonzero coefficients are associated with $Y_{l,0}$, with degrees $l = 0, 2, 4$. The expansion coefficients themselves are given in Appendix B for both the uniform field case and the field of a pointlike charge. Using those expansions, matrix elements of the perturbation are readily evaluated as the product of radial overlap integrals, which depend only on the (v, j) combinations for the two states under consideration, and the angular overlap integrals, which depend only on the (j, m)

combinations and are easily determined via the well-known Wigner-3J coefficients (Appendix B).

Because each of the radial overlap integrals is used many times over—for states with different values of m , for the various coefficients in the spherical harmonic expansion of the perturbation, for investigating different field configurations, and for the dipole moment operator (Section 4) as well as the Hamiltonian—it is computationally efficient to evaluate all integrals of the form

$$\langle \mathcal{T}(v, j; u, k) \rangle = \int dr \mathcal{R}_{v,j}(r)\mathcal{T}(r)\mathcal{R}_{u,k}(r), \quad (3)$$

(where \mathcal{T} stands for any of the 16 independent tensor components) and store the resulting matrices. With only ~ 150 different combinations of (v, j) for each nuclear spin state, the required storage space is modest.

For the field configurations under study in this paper, the spherical harmonic expansion of the perturbation contains only a small number of terms so the Hamiltonian matrix is sparse and can be stored in a compact form. Much more space would be required to store the eigenvectors of the Hamiltonian, which form a dense matrix, so it is preferable to store the Hamiltonian itself; when the eigenvalues and eigenvectors are needed in future, the Hamiltonian can be read from the file system and diagonalized in only a few seconds.

An immediate consequence of axisymmetry in the electric field is that the perturbation only mixes together basis states having the same value of m , because the matrix elements $\langle j, m | Y_{l,0} | j', m' \rangle$ are zero unless $m' = m$. Consequently, the z component of the angular momentum is well defined and m is a good quantum number of the perturbed molecule.

Because the electrical perturbation is not isotropic, there is mixing of basis states with different values of the total angular momentum, and therefore j is not a good quantum number for the electrified states. The fact that the angular structure of the electrical perturbation includes only spherical harmonics with even values of the degree l means that para- H_2 basis states are only mixed together with other para- H_2 basis states, and similarly for ortho- H_2 . Consequently, the ortho- and para-sequences can be analyzed separately, as noted in Section 2.

Finally, there is mixing of different vibrational eigenstates, because none of the off-diagonal elements of the response matrices $\langle \mathcal{T} \rangle$ of Equation (3) are expected to vanish, and therefore v is not a good quantum number of the perturbed molecule. However, for the low-lying rovibrational states, with small v and small j , the energy difference between adjacent vibrational states is large compared with the energy difference between adjacent rotational states and there is much less mixing of vibrational eigenstates than rotational eigenstates (Poll & Hunt 1985).

Our calculations were performed using the *Mathematica*² software package, which provides a facility for obtaining the eigensystem of the Hamiltonian. Despite the large dimensions of that matrix, diagonalization requires only a few seconds on a laptop computer.

An important qualitative aspect of the solutions is that the $(2j+1)$ -fold degeneracy of the unperturbed states is not completely lifted by the electrical perturbation (2): for $m \neq 0$ there remains a two-fold degeneracy associated with the sign of m . Consequently, we will typically not make explicit mention of the $m < 0$ states because their properties are identical to

² <http://www.wolfram.com>

those of the corresponding $m > 0$ states. Furthermore, the electrical perturbation does not mix states of different m values so it is possible to restrict attention to $m \geq 0$ at the outset. Doing so is beneficial because it reduces the size of the basis to only 1861/1828 elements for the para-/ortho- sequences, effecting a factor of a few speedup in the diagonalization of the Hamiltonian. An additional benefit is that the radiative transition rates (Section 4) are easier to interpret in the smaller basis—because the perturbed eigenstates necessarily correspond to a well-defined value of m , rather than a linear combination of $\pm m$ as is the case with the full basis.

3.1. The Perturbed Ground State

To illustrate how an electric field affects the H_2 molecule we show its influence on the rovibrational ground state. The ground state is a useful point of reference because its properties in zero field are already familiar: an isotropic angular distribution of the internuclear axis and a radial wave function that is approximately Gaussian.

The wave function of a perturbed state with eigenvector \mathbf{a} can be written as

$$\Psi = \sum_{v,j} a_{v,j,m} \chi_{v,j}(r) Y_{j,m}(\theta, \phi), \quad (4)$$

and the probability dP of the internuclear vector having length within dr and orientation within a solid angle $d\Omega$ is $dP = \Psi^* \Psi r^2 dr d\Omega$. To obtain either the angular or radial probability density functions (PDFs) we expand $\Psi^* \Psi$ into a double sum and integrate over either the radial or the angular variables, respectively. Because the spherical harmonics are orthonormal the summation simplifies to

$$\frac{dP}{dr} = \sum_{v,j,v'} a_{v,j,m} a_{v',j,m}^* \mathcal{R}_{v,j}(r) \mathcal{R}_{v',j}(r), \quad (5)$$

for the radial PDF. (There is no comparable simplification for the angular PDF.) In practice it is convenient to construct approximate PDFs in which the smallest components of \mathbf{a} are set to zero prior to evaluating the sum, and the results shown in this section were computed using only the largest 300 components.

We have evaluated these PDFs for two different field strengths, $|\mathbf{F}| = 0.01$ and 0.04 atomic units, and for each of the three field configurations under study here: a uniform field, the field of a pointlike charge $q = +e$, and the field of a pointlike charge $q = -e$. For each of the latter two cases the charge is located at separations of $R = 1/\sqrt{|\mathbf{F}|} = 10$ and 5 atomic units ($R \simeq 5.13$ and 2.65 \AA) from the center of mass of the molecule.³

The effect of a uniform field is to align the molecule parallel to the field, as can be seen in the left-hand panels of Figure 1. This is as expected because the polarized state is energetically preferred, and the induced dipole moment is greatest when the field is oriented along the internuclear axis: α_{zz} is significantly larger than α_{xx} , and similarly for the hyperpolarizability γ . The degree of alignment increases as the field strength increases.

When the molecule is near a pointlike charge, the perturbation is influenced by various electric field gradients, as well as the

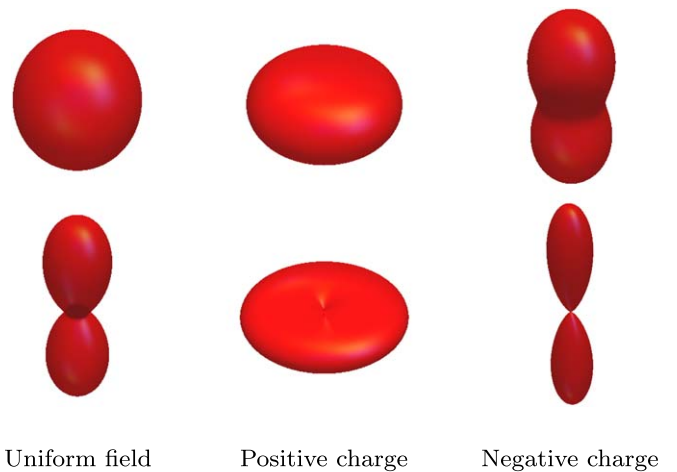


Figure 1. Angular PDFs for the para- H_2 rovibrational ground state in a field of strength 0.01 (upper row) and 0.04 atomic units (lower row). The z -axis (field direction) is vertically oriented in all cases. Left: a uniform field. Middle: a pointlike positive charge. Right: a pointlike negative charge.

field strength, and the angular PDF changes accordingly. Some of the gradient-dependent perturbations—specifically, those associated with Θ , Φ , and B (see Appendix B)—change sign with the sign of the charge, leading to very different angular distributions in those two cases. At low fields the dominant perturbation is the R^{-3} contribution from the permanent quadrupole, and the energetically preferred alignment for this interaction is parallel to the field if the charge is negative (top-right panel of Figure 1) and perpendicular if the charge is positive (top-middle panel of Figure 1). As the separation R is decreased, the other response tensors contribute, but the net effect is simply to enhance the weak-field alignment preferences—as can be seen in lower-middle and lower-right panels of Figure 1.

The influence of the field on the radial distributions is not so pronounced because, as already noted, for the low-lying rovibrational states there is less mixing of vibrational eigenstates than rotational eigenstates. The radial PDFs derived from Equation (5) are presented in Figure 2 (for field strength 0.04), along with that of the unperturbed ground state, showing that the perturbed profiles are all very similar to each other. The main effect of the electrical perturbation is a slight shift of the centroid to larger radii. That can be understood by reference to the plots in Appendix A, which show that, around the location of the ground state, all of the tensor components are increasing in magnitude toward larger radii. It follows that if the electrified state is energetically preferred then the ground state will shift to larger radii. And the perturbed states are indeed energetically preferred. Relative to the eigenvalue for the field-free ground state ($-36,118.1 \text{ cm}^{-1}$, Komasa et al. 2011), the electrified ground states in a field of strength 0.01 (0.04) are located at -59.6 cm^{-1} (-1010.8 cm^{-1}) for a uniform field, -66.4 cm^{-1} (-1300.6 cm^{-1}) for a positive charge, and -69.7 cm^{-1} (-1586.9 cm^{-1}) for a negative charge.

3.1.1. Eigenvector Rotation with Field Strength

Each of the eigenstates of the perturbed molecule can be described as a weighted sum of the unperturbed eigenstates,

$$|\Psi\rangle = \sum_{v,j} a_{v,j,m} |v, j, m\rangle, \quad (6)$$

³ The atomic unit of electric field strength corresponds to approximately $5.14 \times 10^{11} \text{ V m}^{-1}$. For a point charge q and separation R the radial electric field is simply $F = q/R^2$ when all quantities are expressed in atomic units. The fundamental charge $q = e$ is unity in atomic units, so $F = \pm 1/R^2$ for the positive and negative charges considered here.

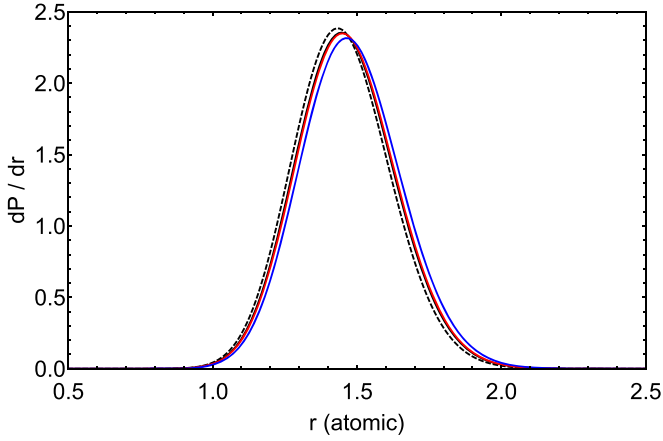


Figure 2. Radial PDFs for the rovibrational ground state of H_2 are as follows: the field-free case, dashed black line; a uniform field, solid black line; positive charge, solid red line; and negative charge, solid blue line. In the electrified cases the field strength is 0.04 atomic units. The distributions are almost identical for a uniform field and for a positive charge. We do not show results for the weaker of the two fields (0.01 atomic units), because all three electrified curves lie on top of the zero-field distribution in that case.

satisfying the eigenvector normalization condition $|\mathbf{a}|^2 = \sum_{v,j} |a_{v,j,m}|^2 = 1$. We can examine the behavior of the coefficients $a_{v,j,m}$, for the ground state of the molecule, as the field strength increases; the evolution is shown in Figure 3 for the case of a para- H_2 molecule in the field of a pointlike negative charge.

At zero field the only nonzero coefficient of the ground state eigenvector is $a_{0,0,0} = 1$, and as the field strength increases that eigenvector gradually moves away from $|0, 0, 0\rangle$ (formally it is a rotation relative to the fixed basis vectors). In Figure 3, therefore, we see $|a_{0,0,0}|$ declining as the field increases, while $|a_{0,2,0}|$ at first grows and then itself declines as the higher rotational states $|0, 4, 0\rangle$ and $|0, 6, 0\rangle$ start to contribute more strongly to the ground state.

3.2. Perturbed Excited States

The influence of an electric field on the excited rovibrational states is qualitatively similar, and we can therefore anticipate some basic trends in the excited states as follows. First, as the total angular momentum of a rotational state increases so does the energy difference between adjacent rotational states. Consequently, for a given strength of perturbation the degree of rotational mixing decreases as j increases. The opposite is true for a vibrational sequence: the vibrational level separation shrinks as v increases, so the degree of vibrational mixing goes up.

Of course the strength of the electrical perturbation is not actually the same along a rotational or vibrational sequence as the tensor components are functions of the internuclear separation (see Appendix A) and the expectation value of the internuclear separation differs from state to state. This change is also systematic in the sense that higher levels of rotational or vibrational excitation correspond to larger internuclear separations and thus all of the tensor components increase in magnitude with increasing rotational or vibrational excitation. This effect is substantial even for the second-rank response tensors, with Θ and α_{xx} reaching values up to about twice that of the ground state and about three times for α_{zz} (depending on the level of excitation). But it can be much larger for the fourth-

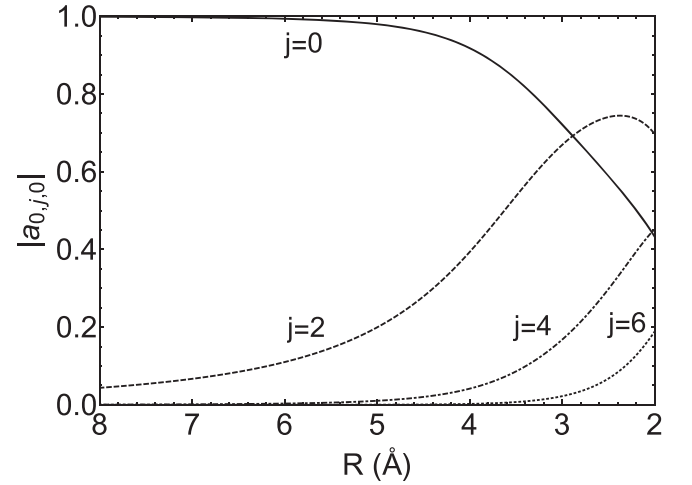


Figure 3. The moduli of the first few coefficients of the ground state eigenvector, for a para- H_2 molecule in the field of a pointlike negative charge, plotted as a function of separation. The different lines show $|a_{0,j,0}|$ for $j = 0$ (solid line); $j = 2$ (dashed line); $j = 4$ (dotted-dashed line); and $j = 6$ (dotted line).

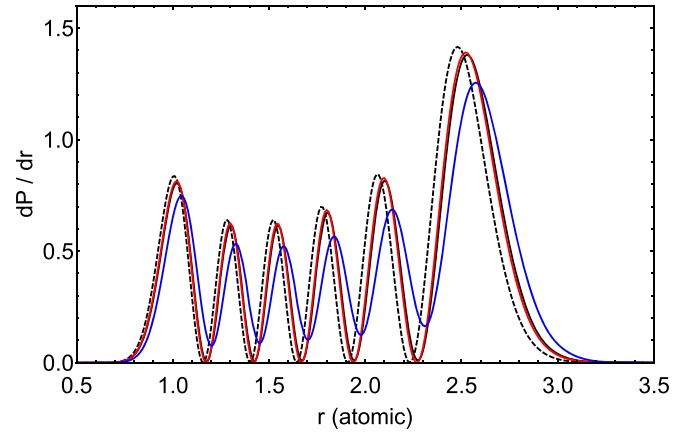


Figure 4. As Figure 2, but for the $|\hat{5}, \hat{0}, \hat{0}\rangle$ state of H_2 .

rank response tensors—particularly γ_{zzz} , which grows by about $20\times$, and E_{zzz} , which grows by about $40\times$ along the vibrational sequence. In combination with the decreasing vibrational quantum noted above, this leads us to expect much greater vibrational mixing in the electrified states as the level of vibrational excitation increases—a trend that has important consequences for the appearance of the ground state absorption spectra (see Section 4).

The stronger mixing of the excited vibrational states is reflected in their radial PDFs, as illustrated with the $|\hat{5}, \hat{0}, \hat{0}\rangle$ state⁴ in Figure 4 ($|F| = 0.04$ atomic units). In that figure we can see a much greater displacement of all the electrified states to larger separations (when compared with the displacement of the ground state seen in Figure 2), and in the case of the negative charge (blue curve) the shape of the PDF is also changed substantially with local minima well above zero. The corresponding angular distributions are all qualitatively similar

⁴ Although v and j are not good quantum numbers for the electrified molecule, they are nevertheless useful for labeling the perturbed eigenstates, and in that context we write them as $|\hat{v}, \hat{j}, \hat{m}\rangle$ in order to distinguish $|\hat{v}, \hat{j}, \hat{m}\rangle$ from the unperturbed eigenstate $|v, j, m\rangle$. Labels are then assigned so that $|\hat{v}, \hat{j}, \hat{m}\rangle$ rotates smoothly to $|v, j, m\rangle$ as the field is decreased smoothly to zero.

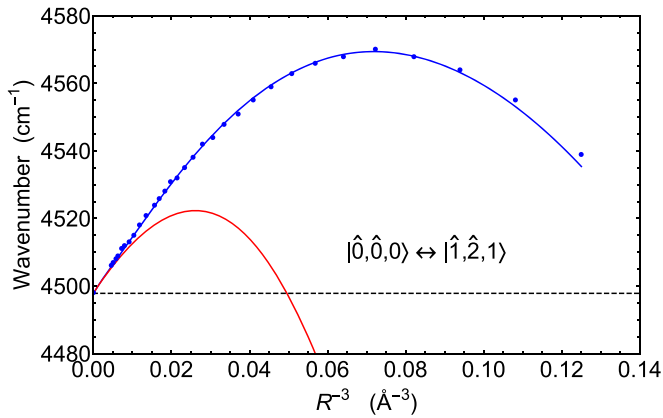


Figure 5. Transition wavenumbers for the fundamental vibrational line of H_2 situated in the field of a pointlike charge $q = +e$, as a function of the (inverse cube of the) separation R between the charge and the center of mass of the molecule. Blue points show the results of Poll & Hunt (1985); the blue line shows our like-for-like calculation (second-rank tensors only). The red line shows our full calculation, including the fourth-rank response tensors. The dashed, black line shows the location of the transition in the field-free case. At large R , the quadrupole interaction dominates and the Stark shift is $\propto R^{-3}$ (see Appendix B).

to examples already shown in Figure 1 as follows: in the case of a positive charge the distribution is similar to the lower-middle panel of Figure 1, whereas the uniform field and negative charge configurations are both similar to the lower-right panel of Figure 1.

3.3. Comparison with Poll & Hunt (1985)

The low-lying electrified states of H_2 have previously been characterized by Poll & Hunt (1985) for one of the field configurations studied here: H_2 in the field of a pointlike charge. In particular Poll & Hunt (1985) calculated the energy levels of 16 low-lying states, for charges situated at various distances between 2 and 6 Å from the molecular center of mass. Their calculations included only the second-rank response tensors, that is, Θ and α , whereas ours include also the fourth-rank response tensors, but they have addressed the same physical situation and it is appropriate to compare our results with theirs.

Quantitatively there are some differences between our results and those of Poll & Hunt (1985) even when we restrict our calculation to the second-rank response tensors in order to effect a like-for-like comparison. At the largest separations considered by Poll & Hunt (1985) our eigenvalues agree with theirs at the level of precision (1 cm^{-1}) that they reported. Decreasing the separation to 3 Å reveals some noticeable differences, of magnitude $\gtrsim 2 \text{ cm}^{-1}$. And as the separation between charge and molecule decreases further, the differences increase rapidly, reaching $\sim 50 \text{ cm}^{-1}$ for a positive charge and $\sim 200 \text{ cm}^{-1}$ for a negative charge at 2 Å. The differences are systematic, with all of our eigenvalues being more negative than the corresponding eigenvalues of Poll & Hunt (1985).

Because the differences between the two sets of calculations are similar across the various eigenstates, the wavenumbers we obtain for transitions are in much better agreement than the eigenvalues themselves. Figure 5 shows an illustrative example: the fundamental vibrational transition of H_2 , $|\hat{0}, \hat{0}, 0\rangle \leftrightarrow |\hat{1}, \hat{2}, 1\rangle$ in the field of a pointlike positive charge. From the figure we can see that our like-for-like calculations agree very closely over most of the range plotted, with the

differences being mainly due to quantization in the Poll & Hunt (1985) values at the 1 cm^{-1} level. At the smallest charge separations the differences are larger but still quite modest at $\sim 4 \text{ cm}^{-1}$. The good agreement we obtain with the results of Poll & Hunt (1985) gives confidence in our solutions.

Figure 5 also shows the results of our full calculation for this transition, including both second- and fourth-rank response tensors. At the time of the Poll & Hunt (1985) analysis there was not enough information available on the fourth-rank response tensors to allow their influence to be gauged. But with the benefit of the recent work of Miliordos & Hunt (2018), and a huge increase in computational resources, it is straightforward to include all of the fourth-rank response tensors and we can now see that they are important. Their contribution is not completely negligible even at a separation of 6 Å, and at 2 Å—where the difference between blue and red curves reaches values $\sim 500 \text{ cm}^{-1}$ —they are an order of magnitude larger than the second-rank contribution to the Stark shift of this spectral line. The rapid divergence of the fourth-rank calculation from the second-rank results, as the charge separation decreases, is understandable: the five extra tensors (Φ , E , C , B , and γ) contribute in proportion to steep powers of the separation, as can be seen in Equations (B7)–(B9), so they are hundreds or thousands of times more important at 2 Å than they are at 6 Å.

One point of practical importance in the case shown in Figure 5 is that the fourth-rank calculation (red curve) predicts a line shift that changes sign between large and small separations. Zero line shift occurs at a charge separation of approximately 2.7 Å, and for separations near that value, this Stark-shifted line would be difficult to distinguish from a zero-field absorption.

4. Absorption Spectra

Given the electrical energy perturbation ΔE of Equation (2), the electric dipole moment of the molecule is

$$\mu_\alpha = -\frac{\partial \Delta E}{\partial F_\alpha} \quad (7)$$

(Buckingham 1967; Bishop 1990; Miliordos & Hunt 2018), which leads to

$$\begin{aligned} \mu_\alpha &= \alpha_{\alpha\beta} F_\beta + \frac{1}{15} E_{\alpha,\beta\gamma\delta} F''_{\beta\gamma\delta} \\ &+ \frac{1}{3} B_{\alpha,\beta,\gamma\delta} F_\beta F'_\gamma + \frac{1}{6} \gamma_{\alpha\beta\gamma\delta} F_\beta F_\gamma F_\delta. \end{aligned} \quad (8)$$

As was the case with the energy perturbation itself, the Cartesian form of the operator is not well suited to rapid evaluation of the corresponding matrix elements. Instead we make a spherical harmonic expansion, leading to the nonzero expansion coefficients listed in Appendix C. Like the Hamiltonian, the resulting matrices are highly sparse and can be conveniently stored in that form, being read in from file when they are needed. To determine the transition dipole matrix elements, that is, $\langle \Psi_1 | \mu_\alpha | \Psi_2 \rangle$ between any two electrified states $|\Psi_1\rangle$ and $|\Psi_2\rangle$, simply requires a rotation of the matrix elements of μ from the unperturbed basis into the perturbed basis. Having evaluated the transition dipole matrix elements, the spontaneous radiative transition rate is given by

(e.g., Atkins & Friedman 2011)

$$A_{21} = \frac{4}{3} \kappa^3 |\langle \Psi_1 | \mu_\alpha | \Psi_2 \rangle|^2, \quad (9)$$

where $\kappa \equiv 2\pi/\lambda$, and atomic units are used throughout. The corresponding Einstein B_{12} absorption coefficient follows naturally, and the radiative lifetime of the upper state is simply the inverse of the sum of the spontaneous radiative decay rates to all lower-lying states, Γ :

$$\Gamma_j = \sum_{i < j} A_{ji}. \quad (10)$$

The spontaneous transition rate given by Equation (9) obviously depends on the orientation of the vector μ_α and thus on the polarization state of the radiation under consideration. We will mostly ignore the polarization properties of the transitions and deal only with the total spontaneous transition rate

$$A_{21} = A_{\parallel} + A_{\perp}, \quad (11)$$

where the parallel component is given by

$$|\langle \Psi_1 | \mu_\alpha | \Psi_2 \rangle|^2 \rightarrow |\langle \Psi_1 | \mu_z | \Psi_2 \rangle|^2 \quad (12)$$

in Equation (9) and the perpendicular component is given by

$$|\langle \Psi_1 | \mu_\alpha | \Psi_2 \rangle|^2 \rightarrow |\langle \Psi_1 | \mu_x | \Psi_2 \rangle|^2 + |\langle \Psi_1 | \mu_y | \Psi_2 \rangle|^2. \quad (13)$$

Although we will not discuss the polarization properties of the transitions, the breakdown into parallel and perpendicular transition rates is given in the numerical results in Section 4.2 for readers who are interested in that aspect.

4.1. Zero-field Absorption Spectra

Before considering the results of our calculations of the rovibrational absorption spectra of electrified H_2 , it is helpful to have a clear picture of the rovibrational spectra of the field-free molecule. The main features of that spectrum are well known (e.g., Herzberg 1950; Turner et al. 1977), but a recent reassessment (Pachucki & Komasa 2011; Rouef et al. 2019) of the contribution of magnetic dipole radiation has led to some significant modifications to the theoretical spectrum. In Figure 6 we show the full spectra of ground state rovibrational transitions, as computed by Rouef et al. (2019), for both ortho- and para- sequences of H_2 .

Although we are interested in absorptions from the ground state, it is simplest to display spectra as the spontaneous transition rates of the upper levels into the ground state—that is, the Einstein A_{21} probabilities per unit time, as shown in Figure 6—rather than the B_{12} coefficients, for example, whose values depend on the convention that is adopted for B_{12} . We will use the same format when displaying the spectra of the electrified molecule in the next section.

Although magnetic dipole can be the principal radiation mechanism for some rovibrational transitions (Rouef et al. 2019), it is a small contribution (much less than 1%) for all transitions connecting to the ground state of ortho- H_2 and zero for all transitions connecting to the ground state of para- H_2 . Thus the qualitative appearance of Figure 6 is entirely familiar, consisting of the $S_v(0)$, $Q_v(1)$, and $S_v(1)$ lines, appearing in groups of the same upper-level vibrational quantum number, v , with $v = 0, 1, 2, \dots, 14$. Anharmonicity in the internuclear potential is reflected in the decreasing spacing between line

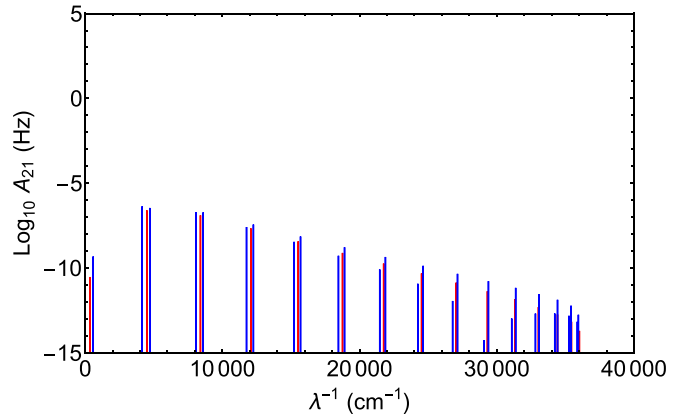


Figure 6. Transitions connecting to the rovibrational ground state for para- (red) and ortho- (blue) H_2 in the absence of an electric field. The line strengths are shown as Einstein A_{21} spontaneous transition rates from the upper level via electric quadrupole and magnetic dipole radiation. All transition properties are taken from Rouef et al. (2019).

groups as the wavenumber is increased and in the nonzero line strengths for transitions to states with $v \geq 2$. However, the level of anharmonicity is low enough that line strengths trend strongly downward as v increases.

4.2. Electrified Absorption Spectra

In the case of electrified H_2 , the molecular states naturally depend on the strength of the static field, and we have therefore determined the energy eigensystem for various values of the field strength: 99 distinct values, equally spaced in the logarithm, for each of the field configurations under study. Rather than quoting the field strength itself, it is more convenient to quote the separation R between the molecule and the pointlike charge when considering that particular field configuration: we determined eigensystems for separations in the range $2 \leq R(\text{\AA}) \leq 8$. In order to facilitate comparison between the different field configurations, in the case of a uniform field we construct an equivalent separation R_{eq} to characterize the electric field strength: R_{eq} is the separation from a pointlike, elementary charge that would yield the same field strength. In all cases we evaluated the electric dipole line strength for each transition, connecting to the ground state of para- H_2 and, separately, ortho- H_2 , using Equations (8) and (9), with the results shown in Figure 7.

Because the electrified molecule has many absorption lines, only the strong ones are displayed in Figure 7; specifically we show only transitions with $A_{21} \geq 10^{-6}$ Hz—a limit that is higher than any of the corresponding transition rates of the field-free molecule (Figure 6). Nevertheless it is clear that a large number of lines lie above that threshold ($\sim 3 \times 10^2$ in each of the para- and ortho- sequences in each of the three panels). Each of the three field configurations shows qualitatively similar spectral structure as follows: In weak fields there is a small number of distinct lines, occurring in groups, whose wavenumbers are almost independent of the field strength and that lie close to the wavenumbers of the corresponding zero-field transitions (Figure 6). In this regime the eigenstates of the electrified molecule are very similar in character to those of the field-free molecule, but the transitions are much stronger because of the electric dipole moment that is induced by the static field. As the field strength increases, new transitions appear in the plot where their A_{21}

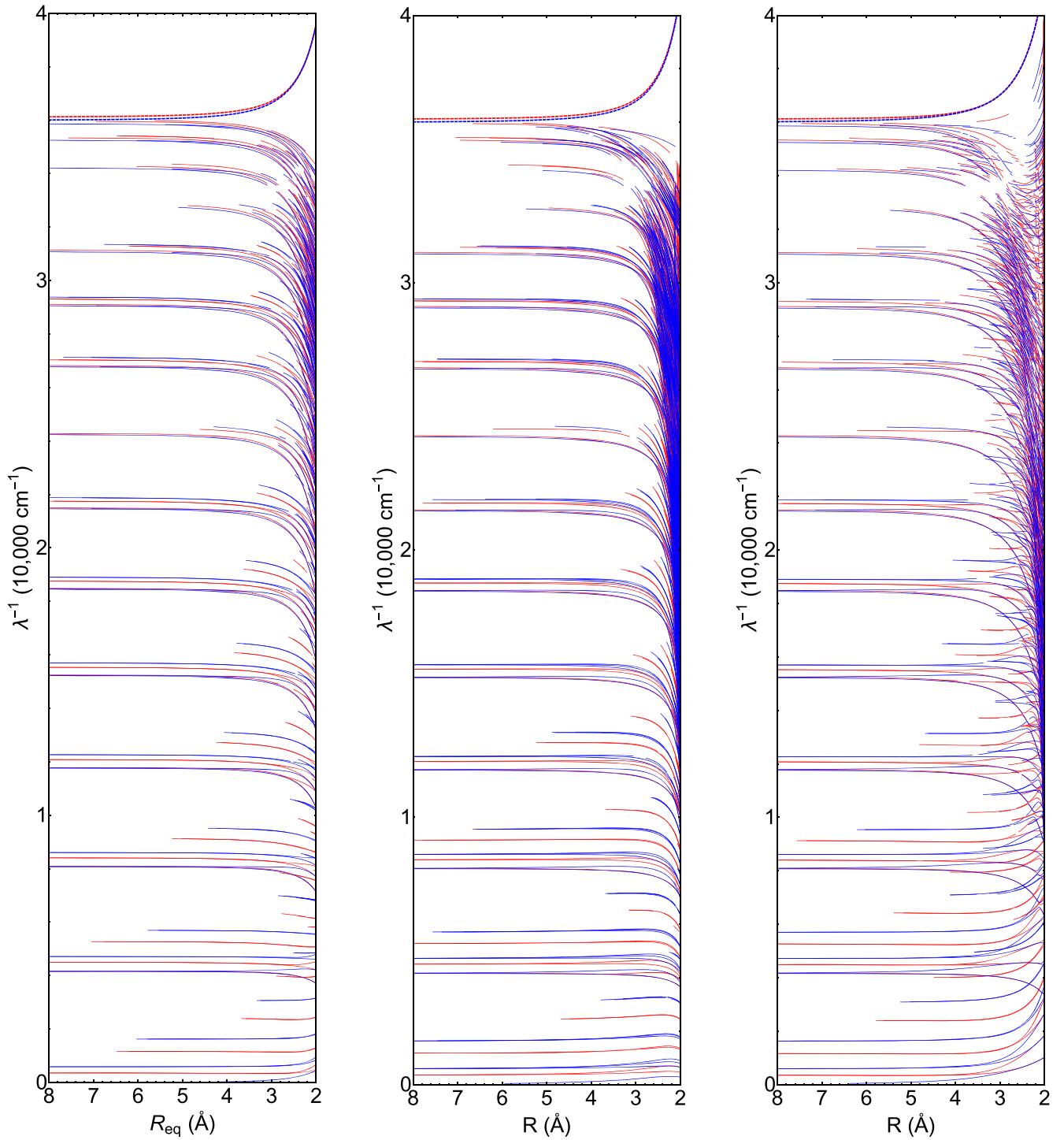


Figure 7. Strong transitions ($A_{21} \geq 10^{-6}$ Hz) connecting to the ground state of electrified H_2 molecules in three different cases: a uniform field (left), the field of a pointlike charge $q = +e$ (middle), and the field of a pointlike charge $q = -e$ (right). Transitions belonging to the para-sequence are shown in red, those belonging to the ortho-sequence are shown in blue, and the location of the continuum is shown with dashed lines of the appropriate color. For each line the wavenumber is plotted (in μm^{-1}) as a function of the separation, R , between the charge and the molecule, for the middle and right-hand panels. For the left-hand panel we use an analogous parameter, R_{eq} , to characterize the strength of the uniform electric field: in atomic units the field strength is $1/R_{\text{eq}}^2$.

values cross our chosen threshold; wavenumbers shift gradually, and degeneracies are lifted because different values of m correspond to different expectation values of the electrical perturbation (2).

In all three panels of Figure 7 we can see examples of transitions moving to both higher and lower wavenumbers as the field strength increases. There are, however, systematic

differences among these field configurations, with the uniform field case and the positive charge both showing a predominance of downward-trending wavenumbers, whereas in the case of the negative charge the distribution between upward- and downward-trending lines is more even. A downward-trending line indicates that the upper level is moving closer to the ground state as the field strength increases.

Table 1
Transitions of H₂ in a Uniform Field

R_{eq} (Å)	$\hat{\nu}$	\hat{j}	m	λ^{-1} (cm ⁻¹)	A_{\parallel} (Hz)	A_{\perp} (Hz)	Γ (Hz)
0.8000000E+01	0	0	0	-0.36129451E+05	0	0	0
0.8000000E+01	0	2	0	0.35349477E+03	0.64426370E-03	0	0.64426370E-03
0.8000000E+01	0	2	1	0.35390320E+03	0	0.48325641E-03	0.48325641E-03
0.8000000E+01	0	4	0	0.11678307E+04	0.78893398E-07	0	0.99479714E-02
0.8000000E+01
0.8000000E+01	0	1	0	-0.36012129E+05	0	0	0
0.8000000E+01	0	1	1	0.17212478E+01	0	0.33195119E-10	0.33195119E-10
0.8000000E+01	0	3	0	0.58730199E+03	0.22994695E-02	0	0.34442652E-02
0.8000000E+01
0.78876298E+01	0	0	0	-0.36130114E+05	0	0	0
0.78876298E+01	0	2	0	0.35344409E+03	0.68172725E-03	0	0.68172725E-03
0.78876298E+01	0	2	1	0.35387604E+03	0	0.51136096E-03	0.51136096E-03
0.78876298E+01	0	4	0	0.11677748E+04	0.93529357E-07	0	0.10527520E-01
...

Notes. Transitions are listed in order of increasing wavenumber, at fixed R_{eq} , first for para-H₂ and then for ortho-H₂; then R_{eq} is decreased and the pattern repeats. There are 99 distinct values of R_{eq} , equally spaced in $\log R_{\text{eq}}$, covering the range $8 \geq R_{\text{eq}}(\text{Å}) \geq 2$. For each combination of R_{eq} and nuclear spin the “wavenumber” of the first line is actually the eigenvalue of the ground state (negative in all cases), with Γ and both A values set to zero. The complete table includes $\sim 3 \times 10^4$ lines and is available as an ascii text file.

(This table is available in its entirety in machine-readable form.)

Table 2
Transitions of H₂ in the Field of a Charge $q = +e$

R (Å)	$\hat{\nu}$	\hat{j}	m	λ^{-1} (cm ⁻¹)	A_{\parallel} (Hz)	A_{\perp} (Hz)	Γ (Hz)
0.8000000E+01	0	0	0	-0.36130078E+05	0	0	0
0.8000000E+01	0	2	1	0.35858861E+03	0	0.48218100E-03	0.48219198E-03
0.8000000E+01	0	2	0	0.36301186E+03	0.68032214E-03	0	0.68032237E-03
0.8000000E+01	0	4	1	0.11753055E+04	0	0.35392560E-05	0.94182994E-02
...

Note. See comments for Table 1, but with $R_{\text{eq}} \rightarrow R$.

(This table is available in its entirety in machine-readable form.)

Table 3
Transitions of H₂ in the Field of a Charge $q = -e$

R (Å)	$\hat{\nu}$	\hat{j}	m	λ^{-1} (cm ⁻¹)	A_{\parallel} (Hz)	A_{\perp} (Hz)	Γ (Hz)
0.8000000E+01	0	0	0	-0.36130214E+05	0	0	0
0.8000000E+01	0	2	0	0.34570893E+03	0.64714783E-03	0	0.64714783E-03
0.8000000E+01	0	2	1	0.34997736E+03	0	0.46922604E-03	0.46922611E-03
0.8000000E+01	0	4	0	0.11603530E+04	0.13245084E-04	0	0.10028004E-01
...

Note. See comments for Table 1, but with $R_{\text{eq}} \rightarrow R$.

(This table is available in its entirety in machine-readable form.)

At the right-hand side of each of the panels in Figure 7 the perturbation introduced by the static field is sufficiently strong that the states of the electrified molecule bear little resemblance to those of field-free H₂, and at wavenumbers above $\sim 1 \mu\text{m}^{-1}$ the spectrum becomes a dense forest of strong lines. Indeed the spectra are so rich that it is difficult to represent all of the information in any plot that covers a range of different field strengths. In the next section (Section 4.3) we will show an example for a specific choice of R where the spectral structure can be seen in detail.

To allow readers to explore any aspect of these spectra that might be of interest, Tables 1–3 present our results for wavenumber, transition probability, and natural line width, Γ from Equation (10), for each transition, for each of the three field configurations, and for each of the 99 field strengths considered. These tables are more comprehensive than the spectra of Figure 7 in two respects: all transitions with probabilities $A_{21} \geq 10^{-12}$ Hz are given, and the transition rates for parallel (A_{\parallel}) and perpendicular polarizations (A_{\perp}) are given separately.

All of the transitions are fully linearly polarized, with our calculated numerical values of the transition rates for one mode being typically 20 orders of magnitude larger than the other; the actual numerical value of the transition probability obtained for the weaker mode is therefore uninteresting and has been set to zero in our tabulations. We note that “parallel” transitions ($A_{\perp} = 0$) are exclusively associated with transitions between states having the same value of m , whereas “perpendicular” transitions ($A_{\parallel} = 0$) involve a change $\Delta m = \pm 1$. That division of polarizations is manifest in Tables 1–3 and is expected on the basis of the spherical harmonic expansion coefficients of the dipole moment operator given in Appendix C.

Because of the two-fold degeneracy in the perturbed levels, corresponding to the two possible signs of m (when $|m| > 0$), we have not reported on $m < 0$ states in Tables 1–3. However, readers must remember those states, and correctly account for them, when making use of these tables. For example, the third line in each table gives $A_{21} = A_{\perp}$ for the transition $|\hat{0}, \hat{2}, 1\rangle \rightarrow |\hat{0}, \hat{0}, 0\rangle$, which implies that there is a corresponding transition $|\hat{0}, \hat{2}, -1\rangle \rightarrow |\hat{0}, \hat{0}, 0\rangle$ with the same wavenumber and A_{21} but which does not appear in the table. The strength of the absorption line at that wavenumber is the combined strength of the two transitions $|\hat{0}, \hat{0}, 0\rangle \rightarrow |\hat{0}, \hat{2}, \pm 1\rangle$.

4.2.1. Eigenvector Rotation and State Labels

As noted earlier, v and j are not good quantum numbers for the electrified molecule, so the values \hat{v} and \hat{j} reported in Tables 1–3 are merely convenient labels. Even so, there is no rigorously correct way of assigning them; our labels have been determined in the following way: In combination, the three quantum numbers $\{v, j, m\}$ uniquely define an eigenstate in zero field. For the weakest field that we considered ($R, R_{\text{eq}} = 8 \text{ \AA}$), the character of the eigenstates is similar to those of the zero-field case, so we simply form the inner product of each of the electrified eigenstates with each of the zero-field eigenstates and transfer the labels from the old to the new according to the magnitudes of those inner products. To ensure the mapping is one-to-one the transfer is done sequentially, starting from the electrified ground state and working up the eigenvalue spectrum and removing each label from the available pool once it has been assigned. This procedure is then repeated, transferring labels from the eigenstates of the weakest field we considered to those of the next-weakest and so on.

If the field is so weak that the perturbed eigenstates are all very close to the unperturbed eigenstates then there is very little ambiguity in the assignment of labels and the procedure described above should yield useful results. However, once the field is strong enough that there is little direct correspondence between the perturbed and unperturbed states, then the choice of labels becomes less clear-cut. Figure 3 shows that we are certainly in that regime for the strongest fields under consideration, because even the ground state $|\hat{0}, \hat{0}, 0\rangle$ has rotated a long way from $|0, 0, 0\rangle$ by the time we reach separations $R \simeq 2 \text{ \AA}$. Moreover, we caution that our coverage of R and R_{eq} —that is, 99 points, equally spaced in the logarithm—might not adequately sample the rotation of the excited state eigenvectors, making it impossible to reliably transfer labels from one field strength to the next.

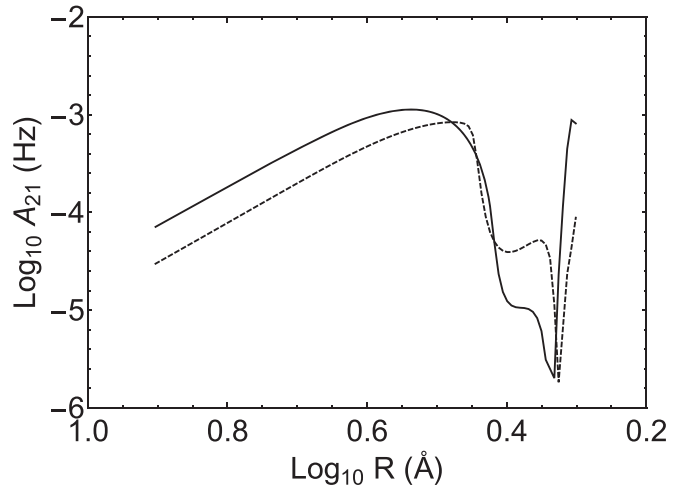


Figure 8. Variation of line strengths with separation from a pointlike charge $q = -e$, for transitions connecting the ground state $|\hat{0}, \hat{0}, 0\rangle$ to $|\hat{3}, \hat{2}, 1\rangle$ (solid line) and $|\hat{4}, \hat{2}, 1\rangle$ (dashed line). At large separations the line strength varies approximately as R^{-4} , whereas at small separations the behavior is complicated, and substantially different between the two lines.

4.2.2. The Dependence of Line Strength on Field Strength

Some simple properties of the field-induced line strengths can be anticipated, according to the following argument. In weak fields the eigenstates can be approximated by the unperturbed eigenstates, so we expect the strongest transitions to arise between two states that have a nonzero value of the electric dipole matrix element in the angular momentum basis, that is, $\langle j, m | \mu_{\alpha} | j', m' \rangle$. Now the values of those matrix elements scale approximately linearly with the electric field strength (the first two terms on the right-hand side of Equation (8)), leading to line strengths that scale approximately as R^{-4} (or R_{eq}^{-4}). That expectation is borne out in practice, as can be seen in Figure 8, where we show two examples for the case of a molecule in the field of a pointlike charge $q = -e$. We also note that the transition wavenumbers are approximately constant in weak fields (see Figure 7), so in that regime the shape of the whole absorption spectrum is fixed and only the overall normalization varies with the field strength.

In contrast to the very simple situation in weak fields, Figure 8 also demonstrates complicated behavior in the line strengths at small separations. Nor is the form of the variation the same for the two lines, and in fact the line ratio crosses unity several times at separations below about 3 \AA . The reasons behind the complicated behavior are easy to understand by reference to Figure 3: in strong fields the eigenvectors of both the ground state and the excited state are changing rapidly, relative to the unperturbed basis, as the field strength increases. That means that the contributions made by the individual dipole matrix elements $\langle v, j, m | \mu_{\alpha} | v', j', m' \rangle$ (i.e., in the unperturbed basis) to the transition dipole $\langle \hat{v}_1, \hat{j}_1, m_1 | \mu_{\alpha} | \hat{v}_2, \hat{j}_2, m_2 \rangle$ must also vary rapidly as the separation changes. Remembering that most of the matrix elements $\langle j, m | \mu_{\alpha} | j', m' \rangle$ are zero (see Appendices C and B), it is no surprise that there are large, nonmonotonic variations in line strength at small values of the separation R .

4.2.3. A Dearth of Bound States near the Continuum

In Figure 7 the continuum levels for para-/ortho- H_2 are shown as red/blue dashed lines near the top of each panel. In all cases we see that the continuum level moves to higher

wavenumbers as the field strength increases, simply reflecting the fact that the ground state becomes more tightly bound with increasing field strength. What is more interesting is that a gap opens up between the highest eigenvalues and the rovibrational continuum, and for strong fields that gap is large compared with the spacing between the eigenvalues. That is true of all three field configurations, but the gap is particularly large for a uniform field and for the field of a positive charge.

It seems likely that this gap is simply an artifact of our model, arising from incompleteness in the basis—a possibility that we advertised at the start of Section 2. The point is that all of the states become more tightly bound when the molecule is situated in an electric field. Presumably, then, states that are unbound in the case of the unperturbed molecule may become bound in the presence of an electric field and would thus fill in the gap. We return to this issue in Section 6.1.

4.2.4. A Very Low Frequency Transition

In the field-free molecule the longest wavelength line is the para- H_2 line $S_0(0)$ at $\lambda \simeq 28 \mu\text{m}$, so given that the Stark shifts are small in weak electric fields we might also expect this to be the longest wavelength line of the electrified molecule. Figure 7 shows that it is not: there is a transition of ortho- H_2 with a wavelength that, in the weak field case, can be *much* longer. Clearly this is not the familiar $S_0(1)$ transition—which is the (blue) line seen, as expected, just above the (red) $S_0(0)$ line in Figure 7—rather it is a “pure orientational” transition, in which only the m value changes: $|\hat{0}, \hat{1}, 0\rangle \leftrightarrow |\hat{0}, \hat{1}, \pm 1\rangle$. (Note that in the case of a uniform field, and also in the case of a negative pointlike charge, the ground state of the ortho- sequence has $m=0$ and the first excited state is the doublet $m=\pm 1$, whereas the reverse is true for the case of a positive charge.) Table 1 shows that in the case of a uniform field with $R_{\text{eq}}=8 \text{ \AA}$, the wavenumber of this transition is only $\lambda^{-1} \simeq 1.72 \text{ cm}^{-1}$; in this instance, however, it is a weak line with $A_{21} \simeq 3 \times 10^{-11} \text{ Hz}$. In each of the three configurations, this line increases in strength and shifts to higher wavenumbers as the field strength increases.

4.3. A Model Spectrum Appropriate to Solvated H^-

In the previous section we presented results spanning a range of field strengths and different field configurations; now we focus on one particular circumstance, allowing us to present the calculated spectrum in more detail. The case we consider here is H_2 in the field of a pointlike negative charge, at a separation of $R=2.7811 \text{ \AA}$ (5.2555 atomic units). This choice was motivated by the results of Wang & Andrews (2004), who concluded that the H^- ion in solvation in condensed H_2 induces a strong line at 3972 cm^{-1} in the ligand molecules; our quoted separation R was chosen to reproduce the wavenumber of that line in our model para- H_2 sequence. This value of the separation should be interpreted as the radius of the first solvation shell of H^- in condensed H_2 .

The full spectrum obtained from our calculation is shown in Figure 9; the line mentioned above is the strongest para- H_2 line in the plot. In fact our model actually produces two lines with almost identical characteristics: $|\hat{0}, \hat{0}, 0\rangle \leftrightarrow |\hat{1}, \hat{0}, 0\rangle$, with $\lambda^{-1} = 3972.0 \text{ cm}^{-1}$ and $A_{21} = 163 \text{ Hz}$, and $|\hat{0}, \hat{1}, 0\rangle \leftrightarrow |\hat{1}, \hat{1}, 0\rangle$, with $\lambda^{-1} = 3971.2 \text{ cm}^{-1}$ and $A_{21} = 164 \text{ Hz}$. Because their properties are so similar, they are superimposed in Figure 9 and only one can be discerned.

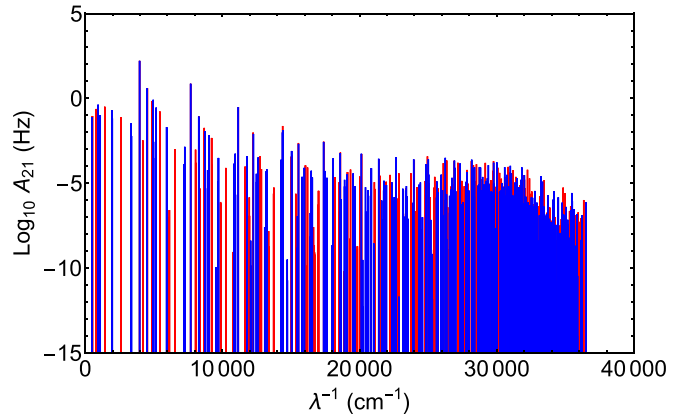


Figure 9. Transitions connecting to the rovibrational ground state for para- (red) and ortho- (blue) H_2 at a distance of $R = 5.2555$ (atomic) from a pointlike negative charge. The line strengths are shown as Einstein A_{21} spontaneous transition rates from the upper level. Note that the scale on both axes is the same as in Figure 6.

The spectrum in Figure 9 is rendered on exactly the same scale as that of the zero-field spectrum shown in Figure 6, demonstrating very clearly that the lines of the electrified molecule are orders of magnitude stronger and more numerous than those of the field-free molecule. In common with the zero-field spectrum, Figure 9 does exhibit a strong decline in line strengths from the fundamental vibrational transition to the overtone lines. Unlike the zero-field case, however, the decline is arrested at about the fifth overtone, with little obvious change in character over the range from 20,000 to 30,000 cm^{-1} .

After the fundamental vibrational lines, the next-strongest transitions seen in Figure 9 are the overtone lines $|\hat{0}, \hat{0}, 0\rangle \leftrightarrow |\hat{2}, \hat{0}, 0\rangle$ and $|\hat{0}, \hat{1}, 0\rangle \leftrightarrow |\hat{2}, \hat{1}, 0\rangle$ at $\lambda^{-1} \simeq 7692.3 \text{ cm}^{-1}$ and $\lambda^{-1} \simeq 7691.2 \text{ cm}^{-1}$, respectively (both with $A_{21} \simeq 7.3 \text{ Hz}$); again, only one of the pair can be discerned by eye. To the author’s knowledge there has been no published report of a strong line near this wavenumber in studies of irradiated solid hydrogen crystals, even though some studies covered this spectral region (e.g., Chan et al. 2000). That is perhaps unsurprising given that the overtone is expected to have less than 5% of the intensity of the fundamental, but it does mean that our spectral model lacks an independent validation.

5. Electrified H_2 in the ISM

In this section we turn our attention to circumstances where the calculations of Sections 3 and 4 are relevant to astronomical observations—that is, manifestations of electrified H_2 in the ISM.

5.1. Condensed Environments

We identify two main circumstances where H_2 could be immersed in a static electric field: a single ion with a small number of H_2 ligands, which we will refer to as a nanocluster, and dust crystals of solid H_2 permeated by electric fields from embedded ions. Broadly speaking, these cases represent the conventional and the unconventional faces, respectively, of condensed H_2 . Whereas nanoclusters are likely to form under conditions that are *known* to exist in the ISM (e.g., Duley 1996), if our Galaxy contains molecular gas that is close to the H_2 saturation curve then, as discussed in the introduction, it would likely have escaped notice.

5.1.1. Nanoclusters

Nanoclusters may form whenever ionic species are present within molecular gas. In practice that means essentially all molecular gas clouds, because there is always some flux of radiation that is energetic enough to penetrate the cloud and cause ionization therein; cosmic-rays are the usual culprits. The resulting chemistry may be complex and interesting, but for our purposes the identity of the ions is less important than the fact that they are able to nucleate the condensation of H_2 . Rates of formation and destruction and the resulting equilibrium abundances, for some types of H_2 nanoclusters, were considered by Duley (1996).

Of all the possible astrophysical manifestations of electrified H_2 , the closest correspondence to our model calculations is the case of a “nanocluster” of one ion and one ligand H_2 molecule. Even in this case, however, our approach is only an approximation. First there is the interaction between the electrons in the molecule and those in the ion, which may contribute positively (repulsion) or negatively (bonding) to the total energy; this interaction is not captured by the description we are using, which is purely electrostatic in nature. Second, even our description of the electrostatics is an approximation because the ions are not simply pointlike charges. Take the H^- ion, for example (Section 4.3): in isolation it is, of course, a spherically symmetric system; but it also has very high polarizabilities (Pipin & Bishop 1992), and under the influence of the electric field from a nearby polarized H_2 molecule it can be expected to develop significant multipolar structure in its own charge distribution. All this is not to say that the results of Section 4 are not useful but that one should not expect a precise correspondence between calculated and observed spectra.

If the nanocluster consists of one ion and several ligand H_2 molecules then, of course, the system is not so well approximated by our calculations. Each of the ligands has induced multipole moments (dipole, quadrupole, etc.), in addition to the permanent quadrupole, hexadecapole, and so on, and these neighboring molecules contribute to the electrical potential structure in the vicinity of the molecule under consideration. Unfortunately, calculating the multipole moments is a difficult task because they depend on the electric fields due to all neighboring molecules, which in turn depend on the multipole moments themselves.

We have not attempted to quantify the mutual couplings just described, but there is a growing literature on *ab initio* structural models of molecular hydrogen nanoclusters, and such models could be used to assess the electrical environments in which the H_2 moieties reside. For nanoclusters of the type $\text{H}^-(\text{H}_2)_n$, structures have been determined using a variety of quantum chemical methods (e.g., Huang et al. 2011; Calvo & Yurtsever 2018; Mohammadi et al. 2020). We note that Calvo & Yurtsever (2018) obtained results in accord with the mass spectroscopy of anion clusters undertaken by Renzler et al. (2016), who demonstrated the existence of “magic numbers” $n = 12$, $n = 32$, and $n = 44$, consistent with icosahedral solvation shells.

Similarly, mass spectroscopy of cation clusters by Jaksch et al. (2008) yielded results consistent with icosahedral solvation shells around the H_3^+ moiety. Unfortunately, there have been no theoretical investigations confirming that interpretation—the largest such nanocluster studied to date includes only four ligand H_2 molecules (Kurosaki & Takayanagi 1998). By contrast icosahedral solvation does not seem to

be favored in the case of the H_3^+ moiety, with the data of Jaksch et al. (2008) apparently indicating a preference for three or six ligand H_2 molecules. The latter preference was evident already in the early work of Clampitt & Gowland (1969). Detailed theoretical modeling of these small clusters has also been undertaken (e.g., Barbatti et al. 2000, 2001).

Although the hydrogenic ions are expected to be important, because hydrogen is the most abundant element, there are many possibilities for forming nanoclusters based on other ionic species—see Bernstein et al. (2013), for example. The most important nonhydrogenic species are presumably those made up of elements with a high abundance, for example, OH^- , and, in the case of cations, a low ionization potential for the parent, such as Li^+ .

5.1.2. Crystals of Solid H_2

There is no clear limit to the number of ligand molecules that can be present before we are obliged to abandon the term “nanocluster” and use instead the name “crystal” or “dust particle,” but a natural division arises where the assembly has more than one ion. As discussed in the introduction, a dust crystal of H_2 in the ISM may have both positive ions and negative ions within the matrix, along with a two-dimensional electron gas trapped on the crystal surface. To some extent, then, we can think of each crystal of solid H_2 in the ISM as being an assembly of nanoclusters of various types. There are, however, some fine distinctions worth noting.

First it is not just the microscopic picture that is relevant. What we might measure in an astronomical context is also dictated, in part, by the overall structure of the condensate—that is, the size and shape of the solid particles. One can imagine a wide variety of possible forms, just as there are many different forms for snowflakes of water ice that are encountered on Earth—dendritic or plate-like or columnar, for example (e.g., Libbrecht 2017). At present, however, we have no useful guidance on these aspects of the astrophysical problem of hydrogen ices, so it seems appropriate to set them aside for now.

Second, in a dust crystal it is possible that the bulk of the molecules are situated in a field that is approximately uniform, whereas this field configuration cannot arise in a nanocluster.

Third, if a large number of nanoclusters are assembled into a dust particle, then a huge number of configurations is possible, and a continuum description of the electrical environment would certainly be required. This is true even if we consider the uniform field configuration noted immediately above, because the field strength will be different in different particles.

5.1.3. Macroscopic Bodies of Solid H_2

This section would not be complete without mention of the possible existence of macroscopic bodies of solid hydrogen. That is not a new idea (e.g., White 1996), but the possibility that we might have actually observed one—in the form of the interstellar object ‘Oumuamua—is a fascinating recent development (Füglister & Pfenninger 2018; Seligman & Laughlin 2020; Levine & Laughlin 2021). Precisely because of their large dimensions, such objects will not contribute significantly to the absorption or emission on typical lines of sight. But if any such object could be identified, it would be very interesting to study it in detail, and the topics aired in this paper are

relevant to the physics of the solid matrix immediately below the surface of the body.

5.2. Lifetime of the Excited States

In Section 4 we evaluated the radiative width Γ of the excited states in each of the configurations under consideration, with the results presented in Tables 1–3. However, for H_2 molecules in a condensed environment it is also possible for the rovibrational energy of the H_2 molecule to flow into the many vibrational modes of the larger complex, rather than into radiation. That mode of decay has the potential to be rapid because the H_2 vibration frequency is very high ($\sim 10^{14}$ Hz), so even a tiny coupling between the rovibrational modes of the H_2 molecule and the vibrational modes of the broader complex would be enough to make internal conversion the dominant deexcitation mode. For example, a 1% probability of decay per oscillation would correspond to a state lifetime ~ 1 ps, whereas the largest value of Γ to be found anywhere in Tables 1–3 corresponds to a radiative lifetime about seven orders of magnitude longer.

When deexcitation occurs via internal conversion the energy could flow down a variety of channels. For example, if the H_2 molecule is adjacent to an H_6^+ molecular ion, the mid-infrared vibrational modes of the latter could be excited. If so, some of the energy absorbed from starlight will reappear as mid-IR line emission from the molecular ion. That is a different pathway to energizing the mid-IR emission of H_6^+ than the electronic excitation envisaged by Lin et al. (2011). Similarly, if the electrified H_2 molecule is part of a dust crystal then, regardless of the electric field configuration, energy can flow into lattice vibrations, thus heating the crystal—a mechanism for powering the far-IR emission of solid H_2 dust from starlight.

5.3. Diverse Electrical Environments

As noted in Section 5.1, electrified H_2 in the ISM could reside in a variety of microscopic electrical environments, and that has implications for how we might observe it. At the very least we are *not* looking for a spectrum such as the one shown in Figure 9, which corresponds to a unique electrical environment, but a sum of several such spectra with weights appropriate to their relative incidence. That type of composite spectrum might arise from nanoclusters of H_2 when the thermodynamics strongly prefer certain configurations. In particular if solvation is only marginally possible then the fraction of ions would be a rapidly decreasing function of the number of H_2 ligands; in that circumstance the composite spectrum might be adequately represented using just the absorption spectra for the one- and two-ligand cases.

However, as nanoclusters may incorporate a large number of ligand H_2 molecules, and each different coordination number implies a slightly different electrical environment (even for the first solvation shell, say), it seems more appropriate to consider the larger nanoclusters as providing a continuum rather than a small set of discrete possibilities. And of course, as commented earlier, charged dust crystals of H_2 manifest a continuum of electrical environments. In turn that means that each of the transitions of electrified H_2 in the ISM should present itself as a broad absorption band rather than a line. Quite how broad can be appreciated by referring to Figure 7 and noting the change in Stark shift for each transition between the weakest field that might be encountered ($R, R_{\text{eq}} \rightarrow \infty$) and the strongest—for

example, $R \simeq 2.8 \text{ \AA}$ for the model of solvated H^- discussed in Section 4.3. Depending on the field configuration and the transition under consideration, that width would be typically in the range 10^2 – 10^3 cm^{-1} .

Such numerous, broad absorption bands would overlap and would in effect contribute to the continuum extinction on any line of sight. Unfortunately, that signature would be very difficult to distinguish from other continuum extinction contributions—for example, the scattering of light from dust particles. A more promising avenue for identifying electrified H_2 is the intraband structure. In other words, each absorption band has a spectral profile that may include some narrow structure at certain wavelengths. Importantly, there can be circumstances in which the transition wavenumber is stationary with respect to changes in the electrical environment, leading to an absorption “caustic”—having the appearance of a spectral line—within the absorption band. In fact numerous instances of turning points $d\lambda/dR = 0$ can be found in Figure 7, and a single example is clearly demonstrated in Figure 5 (red line) at $R^{-3} \simeq 0.026 \text{ \AA}^{-3}$ ($R \simeq 3.4 \text{ \AA}$).

Not all of the transitions shown in Figure 7 exhibit turning points. Unfortunately there appears to be no simple way of anticipating the wavelengths or the specific circumstances under which stationary points will occur: one simply has to calculate. However, it is clear that turning points will not occur in weak fields, because in that case the eigenstates are close to those of the unperturbed molecule and the Stark shifts of all the levels scale in the same way with the strength of the perturbation. For example, at large separations R between molecule and ion the transition shown in Figure 5 demonstrates a simple power-law behavior of the Stark shift ($\propto R^{-3}$) because the quadrupole interaction dominates.

We emphasize that the electrostatic configurations modeled quantitatively in Sections 3, 4 of the present paper are, however, idealized cases. In reality the field would include contributions from all the neighboring molecules in the condensed complex (Section 5.1), and any stationary points would exist within a much larger configuration space. For example, if the calculation is restricted to fourth-rank response tensors, as in the present work, we need 25 parameters to specify the electrical configuration—that is, the coefficients of a multipole expansion of the potential up to the hexadecapole. In practice the monopole is irrelevant (because H_2 has zero net charge), as are two of the dipole coefficients (choice of field direction is arbitrary), so only 22 parameters are required. Even so, that is a large space and a key issue affecting the prominence of any absorption lines is how much of that parameter space is sampled by the condensed H_2 molecules in the ISM.

On that topic it is worth noting that there is at least one situation where the occupied region of the configuration space is effectively one-dimensional, namely the circumstance of a uniform applied field. In that case all of the 22 field coefficients will be nonzero (in contrast to our description in Sections 3, 4), as a result of the permanent and induced multipoles on each molecule in the crystal, but each coefficient depends only on the applied field strength. In this circumstance, with only a single control parameter, any stationary points should yield readily visible absorption lines.

It is important to recognize that the sort of spectrum we have just described—in which lines form only as a result of stationary points—may look very different from Figure 9, say.

For example, the fundamental vibrational line is easily the strongest feature in that spectrum, but if there is no stationary point for that transition, across a broad range of sampled electrical environments, then there will be no absorption line. Instead, the transition will simply appear as a broad band of absorption, and, despite its strength, it might be difficult to detect. Clearly, accurate predictions for the properties of stationary points will be required in order to identify electrified H_2 in the ISM.

5.4. Emission from Condensates

In Section 4.2.4 we pointed out the existence of a pure orientational transition in ortho- H_2 . Because the upper level of this transition is close to the ground state, at least in the case of weak fields, it can be substantially populated by thermal excitation even at the very low temperatures relevant to condensed H_2 . Consequently, this transition has the potential to be an important cooling line for charged H_2 condensates. That is particularly true for nanoclusters, which have a limited number of modes of excitation; we expect this line to be less important as a coolant in the case of dust particles of condensed H_2 , because thermal continuum emission will be present in that case.

The wavelength of this orientational line exhibits a strong dependence on the strength of the electric field, as can be seen in Figure 7. We have already noted (Section 5.3) the likely diversity of electrical environments in the ISM, and because of that diversity the orientational transition can be expected to appear as a low-frequency bump on top of the thermal continuum of any charged H_2 dust particles. As such it may be of interest in connection with the so-called anomalous microwave emission (AME) that is observed from dusty gas clouds in the Galaxy (e.g., Dickinson et al. 2018).

Providing the condensate temperature is high enough that the Boltzmann factor for the upper level is of order unity, it is straightforward to estimate the surface brightness of this orientational transition in terms of N_{ortho} , the column density of suitably electrified ortho- H_2 :

$$I_\nu \sim \frac{1}{3} \hbar A_{21} N_{\text{ortho}}, \quad (14)$$

where we have assumed that the ground state is the $m = 0$ state. Table 1 shows that in a uniform field with $R_{\text{eq}} = 8 \text{ \AA}$ the pure orientational transition has a frequency $\simeq 50 \text{ GHz}$ and it proceeds at a rate $A_{21} \sim 3.3 \times 10^{-11} \text{ Hz}$; we adopt this transition rate as representative for electrical environments that yield a line frequency of several tens of GHz. Now the observed brightness temperature of the AME is approximately 10^{-5} K at a frequency of 25 GHz and a gaseous hydrogen column of 10^{20} cm^{-2} (see Figure 15 of Planck Collaboration et al. 2014), and this surface brightness would require $N_{\text{ortho}} \sim 2 \times 10^{17} \text{ cm}^{-2}$. The fraction of H_2 in ortho- form is expected to be small, but its value is likely set by nonthermal processes and is difficult to predict. At a notional 1% ortho-fraction, the total column of electrified H_2 needed to generate the observed level of AME is about 20% of the gaseous hydrogen column.

The thermal continuum emission itself will also be different for charged versus uncharged H_2 dust particles. The imaginary part of the dielectric constant for pure solid para- H_2 is very small at low frequencies (Kettwich et al. 2015), because the

rotational transitions of H_2 are very weak. As we have seen, those transitions can be many orders of magnitude stronger when the molecule is electrified, leading to much more efficient thermal continuum emission. In turn this makes solid H_2 more plausible as an interstellar dust candidate, because radiative thermal equilibrium can be achieved at a much lower temperature.

5.5. The Diffuse Interstellar Bands

Many of the spectra we exhibited in Section 4 are entirely unlike the appearance of the molecule in zero field. In particular, the dense forest of lines in the near-IR and optical bands that can be seen in Figure 9 would be difficult to assign to H_2 if one did not have the appropriate theoretical template to hand. As the spectra in Section 4 are the first attempt at constructing such theoretical templates it is likely that any optical absorption lines of electrified H_2 , had they been observed in the ISM, would have been incorrectly assigned or simply not assigned. As is well known, there is indeed a large number of interstellar optical/near-IR absorption lines that have not yet been assigned, known collectively as the DIBs (e.g., Herbig 1995; Sarre 2006; Cami & Cox 2014); it is therefore of interest to consider whether the DIBs might be a manifestation of electrified H_2 .

5.5.1. Diffuse Character of the Absorption Lines

The large line widths of the DIBs are a defining characteristic of the phenomenon. In the case of electrified H_2 , short lifetimes for the excited states arise naturally because the molecules are part of a condensed system—as discussed in Section 5.2. In that discussion we considered a notional lifetime of the excited state of $\sim 1 \text{ ps}$, and in that case the implied line width is $\sim 10 \text{ \AA}$ for a transition in the violet part of the spectrum. That is comparable to the width of 12.3 \AA reported by Jenniskens & Désert (1994) for the strong DIB at $\lambda_{\text{air}} = 4428 \text{ \AA}$.

5.5.2. Number and Distribution of Transitions

The survey spectra reported in Section 4 exhibit hundreds of strong transitions for each field configuration and each nuclear spin state. Thus, even though we are dealing with the simplest of molecules, the level of spectral complexity exhibited by electrified H_2 appears sufficient to account for the hundreds of DIBs that are now known (e.g., Jenniskens & Désert 1994; Hobbs et al. 2008, 2009). Only a handful of the known DIBs lie in the infrared at wavelengths $\lambda \gtrsim 1 \mu\text{m}$ (Joblin et al. 1990; Geballe et al. 2011), and electrified H_2 also shows relatively few transitions in that region (Figure 7).

At the other end of the spectrum, no DIBs are known shortward of about $0.4 \mu\text{m}$ (e.g., Jenniskens & Désert 1994; Herbig 1995). The lack of DIBs in the far-UV (Snow et al. 1977; Seab & Snow 1985) causes no difficulty because such photons lie in the H_2 rovibrational continuum. However, in the near-UV the situation is different: all of our models are rich with transitions down to at least the atmospheric cutoff at around $0.3 \mu\text{m}$, and that is a clear discrepancy between model and data. It may be possible to reconcile this difference when allowance is made for the lifetime of the excited states, as discussed in Section 5.2: higher levels of excitation correspond to larger internuclear separations of the H_2 , leading to stronger interactions with near neighbors and thus a faster redistribution

of energy within the vibrational modes of the condensed complex. In other words, it is possible that near-UV DIBs do exist but have not been detected because they are much broader than the optical and near-IR DIBs.

5.5.3. Line Assignments

In the context of interstellar absorptions, we have already noted that electrified H_2 is likely to give rise to very broad bands, with “lines” appearing only where the transition wavelength is stationary with respect to the field parameters. In principle the stationary points can be determined and the properties of the resulting lines can be compared to those of the DIBs. However, as discussed in Section 5.1 (see also Section 6.1), the models presented in this paper are rather crude representations of the real systems, and we are not in a position to undertake meaningful calculations.

5.5.4. Line Strengths

It is useful to establish an estimate of the quantity of material that would be required to explain the DIBs. If the column density of electrified H_2 molecules is N_{mol} , foreground to a particular source, then the resulting dimensionless equivalent width ($W \simeq W_\lambda/\lambda_0$) of a line with wavelength λ_0 is

$$W \sim N_{\text{mol}} \frac{\lambda_0^3}{8\pi c} A_{21}, \quad (15)$$

where we have neglected the (of order unity) ratio of degeneracies of the upper and lower levels. At a reddening of $E(B - V) = 1$, a moderately strong DIB with $W_\lambda \sim 50 \text{ m}\text{\AA}$ and $\lambda_0 \sim 5000 \text{ \AA}$ would require a column $\sim 6 \times 10^{19}/A_{21} \text{ cm}^{-2}$. That figure is for the molecules that are responsible for the absorption line. But if the line is showing us only those absorptions whose wavelengths are close to a stationary point, then the total column density will be much larger; for the purpose of obtaining numerical estimates we assume that the total column is 10 times larger.

Although electrification leads to H_2 rovibrational lines that are orders of magnitude stronger than in the field-free case, they are nevertheless still quite weak. Taking $A_{21} \sim 10^{-2} \text{ Hz}$ as an estimate of the transition rate for one of the stronger transitions of electrified H_2 —see Figure 9—we arrive at $N_{\text{mol}} \sim 6 \times 10^{22} \text{ cm}^{-2}$ for $E(B - V) = 1$ ($A_V \simeq 3$). We return to this result in Sections 6.3 and 6.4.

5.5.5. Variations in DIB Line Ratios

It is now firmly established (Cami et al. 1997; McCall et al. 2010; Friedman et al. 2011) that the pairwise correlation coefficients between DIBs are broadly distributed and sometimes quite low (e.g., $\lesssim 0.5$); they are rarely stronger than 0.95. By contrast one would normally expect near-perfect correlations among all lines arising from the ground state of a given carrier, so the poor correlations that are observed have to date been interpreted as a requirement for multiple species of carrier. In that case a large number of different carriers, comparable to the number of observed DIBs, is implied. In the case of electrified H_2 , however, we have argued that observed absorption *lines* arise from particular electrical environments where the wavelength is stationary with respect to small changes in those environments. Each such line arises from a different stationary point, corresponding to a different

environment, and the observed line strengths therefore reflect the different populations of the same molecule in the vicinity of the various different points. Those populations are not expected to be tightly correlated, so in the case of electrified H_2 all of the DIBs could in principle arise from just the one carrier.

The degree to which populations in the various different electrical environments might be correlated will depend strongly on the true dimensionality of the electrical configuration space. As noted in Section 5.3, 25 parameters are required to uniquely specify the electrical environment up to the hexadecapole of the potential, but for many physical models there are strong correlations between those parameters, and consequently the true dimensionality of the electrical parameter space can be much smaller. For example, in the case of a uniform field applied to a crystal of H_2 , all of the potential multipoles are fixed by the applied field strength, so the parameter space is only one-dimensional. In that case the strength of the correlation between a pair of lines ought to reflect mainly the difference in field strength of the two stationary points, because the grains ought to be smoothly distributed in field strength. In order to predict the DIB–DIB correlation matrix, however, it will be necessary to identify both the general character of the electrical environments—for example, a crystal with a uniform applied field, or an H_2 nanocluster centered on a single ion—and the astrophysics that governs the statistics of those environments.

6. Discussion

6.1. Limitations of the Model Calculations

Our calculations provide a more accurate characterization of electrified H_2 than has been available to date (Poll & Hunt 1985), but our model is nevertheless far from ideal in some respects. First, although the inclusion of all the fourth-rank response tensors has only recently become possible—and thus represents the state of the art for calculations of this type—there is no reason to think that fourth-rank suffices; it is rather the opposite in fact. A comparison between second-rank and second- plus fourth-rank response is shown in Figure 5 (Section 3.3) for the particular case of the wavenumber of the $|\hat{0}, \hat{0}, 0\rangle \leftrightarrow |\hat{1}, \hat{2}, 1\rangle$ transition for H_2 near a positive elementary charge. In that case we can see that the fourth-rank contribution is small compared with the second-rank contribution only for separations $R \gg 2.7 \text{ \AA}$. However, in the case of the H_6^+ ion, for example, the calculations of Kurosaki & Takayanagi (1998) indicate that the first H_2 solvation shell has a radius of approximately 2.7 \AA . Furthermore, as noted in Section 3.2, the fourth-rank response tensors typically become more important relative to the second-rank contributions as the level of excitation increases. Consequently the sixth and higher rank response tensors would likely be even more important if we are seeking an accurate description of optical absorption lines, rather than the fundamental vibrational line shown in Figure 5.

The situation we have just described is likely to be common to the first solvation shells of other small ionic species, regardless of the sign of the charge. For example, in Section 4.3 we presented a model for H_2 in the vicinity of the H^- ion, designed to match the measured wavenumber of the fundamental vibrational line, for which the preferred separation was determined to be $R \simeq 2.8 \text{ \AA}$. Thus we expect the fourth and

higher rank tensor contributions to be important in this context also.

Unfortunately, the sixth-rank response tensors are even more numerous than the fourth-rank ones—a total of 11 additional tensors, including the permanent 64-pole moment, the octupole polarizability, the fourth dipole hyperpolarizability, and so on. They would also be more challenging both to evaluate *ab initio* and to work with in modeling the eigensystem of electrified H_2 . As these difficulties would be further magnified for the higher-rank response tensors (i.e., rank 8 and above), further expansion of the electrical response model does not seem to be a promising approach to achieving higher accuracy in the strong electric fields under consideration here.

A second concern is that the bound rovibrational states of the unperturbed system may not suffice to describe the states of the electrified molecule, that is, our basis is incomplete. This concern is justified, as noted in Section 4.2.3: the energy eigenvalues become systematically more negative with increasing field strength, and in strong fields a gap opens up between the least-bound state and the continuum. This suggests that states in the unbound continuum of the field-free molecule may become bound when a field is applied.

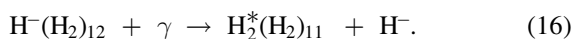
Both of the aforementioned problems have their origin in the fact that the electric fields under consideration include quite large values, for which the electrical energy is not really a small perturbation. It therefore seems likely that a different calculation framework would be more appropriate for further investigation of the properties of electrified H_2 , at least at the upper end of the range of field strengths that we have considered. That idea is strongly reinforced by the fact that our description is purely electrostatic and completely neglects all other interactions between the H_2 molecule and an adjacent ion. By contrast all of the methods of theoretical quantum chemistry are designed to correctly describe such interactions and the strong electric fields that are encountered. What is needed now is quantum chemistry rather than quantum physics.

Notwithstanding the limitations of the model we have used, a great merit is that it furnishes us with a (nearly) complete set of rovibrational transitions for electrified H_2 . Quantum chemical calculations, on the other hand, have to date been more oriented toward understanding aspects such as the binding energy, the geometry, and the fundamental vibrational and rotational transitions—high levels of rovibrational excitation are not routinely characterized.

6.2. Absorptions into the Continuum

All of the transitions reported in Section 4 involve upper levels that are bound states of the electrified H_2 molecule, but presumably there are also allowed transitions that lead to states in the rovibrational continuum. We have not attempted to characterize those transitions so we cannot say much about their properties, but it is interesting to consider where the threshold of that process might lie.

To be specific we take the case of the hydrogen anion with a single, complete solvation shell, that is, $\text{H}^-(\text{H}_2)_{12}$. Absorption of a UV photon can directly dissociate one of the ligand H_2 molecules, via the reaction



In this process the polarization of the dissociating molecule increases to a point where the dissociation products are H^+ and H^- , the latter escaping from the complex and the former

bonding with the central H^- to yield H_2^* , that is, a highly vibrationally excited H_2 molecule. The H_2^* will be close to the dissociation limit, because the constituent atoms have come together from an initial, widely separated state, so its energy relative to the ground state will be approximately 4.5 eV. The H^- that escapes the complex has some kinetic energy, but that ought to be small near the threshold of the process.

The H_2 molecules that are clustered around the H_2^* will also disperse to infinity, because once the charge has been removed from the center they are all unbound. The interaction energy can be estimated from the pairwise interaction potential evaluated at their initial separation—that is, at the radius of the first solvation shell around H^- , which is approximately 2.8 Å (Section 4.3). From the isolated pair interaction potential of Figure 4 in Silvera & Goldman (1978) we estimate the total potential energy of the 11 remaining molecules as roughly +0.2 eV. The total energy of the reaction products is thus approximately +4.7 eV.

By contrast the total energy of the $\text{H}^-(\text{H}_2)_{12}$ cluster is negative: the cluster is bound. The results of Mohammadi et al. (2020) indicate a binding energy per ligand of approximately 1.4 kcal mol⁻¹ for $\text{H}^-(\text{H}_2)_5$, which is the largest cluster they studied. Adopting that figure for all 12 of the ligands in the first solvation shell then implies a total binding energy of approximately 0.7 eV. We therefore require a photon whose energy is at least 5.4 eV in order to initiate the reaction (16). That threshold energy corresponds to $\lambda \simeq 2300$ Å: close to the central wavelength of the UV bump (2175 Å) that is commonly seen in the interstellar extinction curve (e.g., Draine 2003), and the reaction (16) may be of interest as a possible contribution to that feature.

6.3. Electrified H_2 as a DIB Carrier?

In Section 5.4 we proposed electrified H_2 as a DIB carrier, on the basis of several features of the absorption system that are in accord with the properties of the DIBs, but some potential difficulties for that proposal come to mind, as we now describe.

6.3.1. Multiple Carriers versus Just One

A great variety of carriers have been proposed for the DIBs, as discussed in, for example, Herbig (1995), Sarre (2006), and Cami & Cox (2014). There has even been a prior suggestion that H_2 might be responsible for many of the lines (Sorokin & Glowina 1995, 1996), although Snow (1995) has raised objections to some aspects of that proposal. Almost all of the suggested carriers have subsequently been eliminated by dint of a spectral mismatch between laboratory and astronomical data. But there is one candidate molecule, C_{60}^+ , the Buckminsterfullerene cation—suggested by Foing & Ehrenfreund (1994)—that remains viable. Recent data from both laboratory and telescope have strengthened the case in favor of C_{60}^+ being a DIB carrier, with multiple transitions exhibiting a close wavelength correspondence to near-IR DIBs (Campbell et al. 2015; Cordiner et al. 2019). How, then, should we view those assignments in the context of the broader DIB interpretation being advanced in this paper?

At present there is no conflict between electrified H_2 and the C_{60}^+ identifications because we do not have accurate predictions of line locations and strengths for the former. It is possible that electrified H_2 will prove unable to reproduce the locations and strengths of the DIBs that have been assigned to C_{60}^+ , making

the latter species complementary to the former. In that case the result would be a more complex picture than if all the DIBs could be explained by electrified H_2 , but there is no fundamental difficulty with such a composite model. Furthermore, the number of DIBs that can potentially be attributed to C_{60}^+ is less than 1% of the total number known, so the motivation for considering electrified H_2 is hardly diminished at all. Indeed, that would remain true while the origin of the bulk of the DIBs remains uncertain, even if additional carriers were identified in the future. In that case electrified H_2 would be simply one carrier among many, albeit one with the potential to account for a large number of lines.

It also remains a possibility that C_{60}^+ will turn out not to be responsible for the DIBs that have been attributed to it. There are reasons to be cautious about the assignment. First, the astronomical data exhibit substantial structure in the “continuum” in the vicinity of the DIBs in question, making it difficult to measure line centroids and equivalent widths accurately. Second, because DIBs are very numerous and their profiles are broad, individual wavelength coincidences have a nonnegligible probability of arising purely by chance. A simultaneous match for several wavelengths, as demonstrated for C_{60}^+ , is highly improbable when considered in isolation, but it becomes much more likely when viewed as the outcome of a process in which a large number of candidate carrier species are considered and unsuccessful candidates are discarded. These comments are not intended to disparage the C_{60}^+ assignments but to encourage readers to give serious consideration to the possibility that all of the DIBs might be attributable to a single carrier.

6.3.2. Interpretation of Diffuse Band Profiles

Although some DIBs are consistent with Lorentzian profiles, others are known to show substructure. For example, the 6614 Å DIB shows multiple peaks with small separations; these have been interpreted as rotational substructure arising from a large molecule with a rotational constant in the range $0.003 \lesssim B(\text{cm}^{-1}) \lesssim 0.02$ (much smaller than that of H_2 ; Sarre et al. 1995; Kerr et al. 1996). The question then arises as to how the $\sim 1 \text{ cm}^{-1}$ splitting that is observed for the 6614 Å DIB, for example, might be interpreted under the hypothesis that electrified H_2 is the carrier? Certainly the scale of the substructure is not comparable to either the rotational or vibrational line separations of H_2 —which are hundreds or thousands of cm^{-1} , respectively. One possibility is that electrified ortho- H_2 lines might exhibit small splittings due to hyperfine interactions between the nuclear spin $I = 1$ and the nuclear angular momentum j ; such interactions are not included in our Hamiltonian (2). Thus, although we have not demonstrated transition multiplicity akin to that seen in some of the DIB data, it should not be assumed that electrified H_2 cannot exhibit such splittings.

6.3.3. DIBs Correlate Strongly with H I

The fact that DIB equivalent widths are known to correlate strongly with the atomic hydrogen column density and only weakly with the (gaseous) molecular hydrogen column density (e.g., Herbig 1995) is an obvious issue that needs to be faced up to. There are, however, some good reasons to think that this is not a fundamental incompatibility. First, in the ISM, electrified H_2 can only occur in condensates, not in the gas phase, and it is

not at all clear what relationship should be expected between the column densities of H_2 in the two forms. As they are different thermodynamic phases of the same substance, one might even expect there to be an anticorrelation, with the dominant form being determined by the local thermodynamic conditions. Second, as emphasized in the introduction, any gaseous H_2 that is cold and dense enough to permit precipitation of the pure solid is likely to have escaped detection to date (e.g., Pfenniger et al. 1994; Gerhard & Silk 1996; Walker & Wardle 2019). In other words, at present we might not be measuring the largest contribution to the gaseous molecular hydrogen column. Third, we recall the suggestion by Allen & Diaz-Miller (2004) that diffuse atomic hydrogen may arise as a result of UV photodissociation of uncatalogued H_2 . That idea seems particularly attractive in view of the large column of electrified H_2 that we estimated would be required to explain the measured DIB strengths (Section 5.5.4, but see also Section 6.4).

In addition to the strong correlation between DIB equivalent widths and H I, weaker correlations with H_2 have been demonstrated by Lan et al. (2015), with sufficient precision to reveal different dependencies for different lines. It was shown by Lan et al. (2015) that modeling DIB strengths as power laws in both $N(\text{H I})$ and $N(\text{H}_2)$ yields a compact description that captures several aspects of DIB phenomenology—phenomenology that had previously been described in different terms. To connect that description to the present paper we suggest that the two gas column densities are not themselves the fundamental variables that determine DIB strength but that those column densities provide gauges of the interstellar conditions that do determine DIB strength. In particular we note that the UV radiation field is expected to play an important role in grain charging, as well as in converting H_2 to H I, so the key ingredients could be the UV field and a supply of condensed hydrogen.

6.3.4. A Solid-state Carrier?

The possibility that the DIBs might arise in dust grains is not a new idea. Quite the opposite in fact: the correlation between dust reddening and DIB equivalent widths made solid-state carriers an early focus of attention in the history of DIB research (e.g., Herbig 1995). But the prevailing view at present is that the carriers are more likely to be molecules in the gas phase. Snow (2004) summarized the main evidence against a solid-state carrier of the DIBs in four key points: (1) the DIBs show little or no profile or wavelength variations, even among lines of sight showing a variety of dust extinction characteristics; (2) the DIBs show none of the “emission wings” that were anticipated for absorption lines arising from dust particles; (3) there is little or no variation in polarization across individual DIBs; and (4) some of the DIBs are much narrower than typical solid-state transitions.

The last of those points is clearly not a compelling argument because there is no requirement for the DIBs to be “typical solid-state transitions.” In fact solid para- H_2 is far from being a typical solid; in its pure form it is used for matrix isolation spectroscopy of small molecules precisely because the line widths can actually be even narrower than in the gas phase (e.g., Fajardo et al. 2009).

The difficulties posed by points (1) and (2) only apply to a subset of interstellar dust particles—depending on the refractive index and particle size/shape. In our case the relevant

refractive index is unknown, but a useful fiducial refractive index is that of pure, solid para-H₂, which in the optical has the approximate value 1.13 with a very tiny imaginary component (Kettwich et al. 2015). For small particles with refractive index close to unity Rayleigh–Gans theory applies, and spheres with radius small compared to the wavelength exhibit absorption line profiles that are indistinguishable from molecules in gas phase (Section 11.41 of van de Hulst 1981). Not just spheres, in fact: for small particles with refractive index close to unity the influence of shape is simply that of a “form factor” that affects the overall normalization but not the spectral profile of an absorption line (chapter 6 of Bohren & Huffman 2004). For this entire class of hydrogen dust particles, then, no variation in the wavelength or profile of absorption bands can arise from the particulate nature of the carrier. Similarly, for that class of particles, there is no apparent emission on the wings of the line. Small particles also dodge the polarization bullet of point (3): Whittet (2004) states that the observed polarization of starlight arises almost entirely in the large grain population.

The arguments mustered above demonstrate that there is at least one possible manifestation of H₂ condensates that satisfies the known constraints on solid-state DIB carriers—namely, subwavelength particles. It is possible that there might be other manifestations of solid H₂ that could meet the known constraints, but it is beyond the scope of this work to explore that possibility.

6.3.5. Relationship of the DIBs to Other Observables

A tighter grain size limit can be determined by considering the implied extinction due to scattering. In Section 5.5.4 we estimated that a column $N_{\text{mol}} \sim 6 \times 10^{22} \text{ cm}^{-2}$ of electrified H₂ would be required to generate the DIB strengths seen at a visual extinction of about three magnitudes. For spherical hydrogen grains of radius a this molecular column translates into a grain column of $N_{\text{grain}} (\text{cm}^{-2}) = (a/0.82 \text{ cm})^{-3}$. And if the real part of the dielectric constant is similar to that of pure, solid para-H₂ ($\epsilon \simeq 1.27$, Kettwich et al. 2015), then each grain has a scattering efficiency (i.e., cross-section in units of πa^2) of $Q_{\text{sca}} \simeq 30(a/\lambda)^4$ (Equation (5.8) of Bohren & Huffman 2004). It follows that $A_V < 3$ requires $a \lesssim 100 \text{ \AA}$. We note that this limit does not automatically prefer isolated nanoclusters over dust crystals because the smallest individual nanoclusters have radii $\simeq 3 \text{ \AA}$.

In view of the low levels of optical absorption in pure solid para-H₂, the transitions giving rise to the DIBs should dominate the optical absorption in charged grains. Consequently the measured properties of the DIBs themselves can be used to estimate the resulting absorption. We use a Lorentz oscillator model to approximate⁵ the imaginary part of the dielectric constant of the ISM in terms of the measured properties of the known DIBs: the central frequency, ν_j ; the corresponding FWHM, γ_j ; and the dimensionless equivalent width, W_j . That model gives a total absorption optical depth of

$$\tau(\nu) = \frac{6}{\pi} \text{Im} \sum_j \frac{W_j \nu_j \nu}{\nu_j^2 - \nu^2 - i \nu \gamma_j}, \quad (17)$$

with no adjustable parameters. Taking the properties of the 378 DIBs reported by Hobbs et al. (2008), which correspond to a line of sight with $E(B - V) \simeq 1$ ($A_V \simeq 3$), we find that the

absorption in V band has a floor at $\tau \sim 10^{-4}$. That is too small to account for a continuum extinction of $A_V \simeq 3$. However, in our preferred interpretation each of the DIBs is only a fraction of a stronger and *much* broader absorption band of electrified H₂. To obtain a rough, quantitative estimate we assume that (1) each observed DIB manifests only $\sim 10\%$ of the total strength of each absorption band and that (2) the full width of each band is $\gamma_j \sim \nu_j/20$. With these assumptions, the V-band optical depth is a few percent, still too small to explain the continuum extinction that is observed but not completely negligible.

The foregoing estimates suggest that there may be scope for accommodating electrified hydrogen as an addition to conventional dust models based on silicates and carbonaceous grains, with the former accounting for the DIBs and the latter accounting for the observed continuum extinction. But a simpler model might be possible, in which charged hydrogen grains also account for the bulk of the continuum extinction. That simplicity is appealing, but a viable dust model based exclusively on H₂ condensates has not yet been demonstrated, and the requirements for a successful model go well beyond just extinction—see, for example, Draine (2003).

We have already noted (Section 5.4) a possible connection between the pure orientational transition of electrified ortho-H₂ and the AME that is observed from dusty regions of the Galaxy. But it is known that AME is tightly correlated with the far-IR thermal emission from dust (e.g., Hensley et al. 2016), so ideally one would like to have a model in which both of these radiations arise from the same particles. Thus a better understanding of charged H₂ grains would be of interest not only in connection with the DIBs but also with the continuum extinction, AME, and the far-IR emission.

6.4. Total Mass of Electrified H₂

In Section 5.5.4 we estimated that $N_{\text{mol}} \sim 6 \times 10^{22} \text{ cm}^{-2}$ in charged hydrogen grains would be required to explain the observed DIB strengths at a reddening of $E(B - V) = 1$. By contrast the expected column of diffuse gas at this reddening is much smaller: $N_{\text{H}} \simeq 6 \times 10^{21} \text{ cm}^{-2}$ (e.g., Draine 2003). This remarkable situation, in which the dust outweighs the gas by a factor ~ 20 , is opposite to the hierarchy that applies in conventional (silicate + carbonaceous) dust models, where the grains amount to only $\sim 1\%$ of the gas mass. As can be seen from the way N_{mol} is calculated in Section 5.5.4 the large total grain mass that we infer follows directly from the fact that, despite electrification, the rovibrational transitions are not very strong.

Although such a large mass in dust is initially surprising, it is not entirely unwelcome. Galaxies contain a great deal more mass than can be seen in stars and diffuse gas (e.g., the many contributions to Ryder et al. 2004), so there is certainly scope in the dynamics for a substantial mass in H₂ grains. Furthermore, the fact that DIB strengths are well correlated with the H I column (Section 6.3.3) means that the contribution of the DIB carriers to galaxy rotation curves is simply a scaled version of the contribution of the H I itself, and it is known that much of the observed structure of rotation curves can be accommodated by simply scaling the contributions of the stars and the diffuse gas (Swaters et al. 2012, and references therein).

Despite its dynamical appeal we can rule out the possibility that such a large mass resides in small particles of condensed H₂. Material in the ISM is bombarded by cosmic-rays, resulting

⁵ As noted in Section 6.3.2, not all of the DIB profiles are Lorentzian.

in γ -ray emission via bremsstrahlung and pion production, and these diffuse, Galactic emissions have been studied by a succession of satellite instruments since the 1970s (e.g., Kraushaar et al. 1972; Hunter et al. 1997; Ackermann et al. 2011). The observed γ -ray intensities are similar to those calculated on the basis of the independently measured cosmic-ray spectra and the spectral-line surveys of the molecular and atomic gas content of the Galaxy, and this similarity in absolute normalization excludes the possibility that the interstellar dust in the diffuse ISM is 20 times more massive than the diffuse interstellar gas.

There are, however, some substantial systematic uncertainties involved in the calculation of diffuse γ -ray emissions, so this avenue of constraint does not oblige us to accept a dust mass that is as small as the $\sim 1\%$ (of the gas mass) that is usually assumed. Several factors entering into the calculation are uncertain by $\gtrsim 10\%$ (Delahaye et al. 2011), including the relationship between the local interstellar cosmic-ray spectra and the spectra measured inside the heliosphere (Cumplings et al. 2016), the spatial variation of cosmic-ray spectra within the Galaxy (Strong et al. 2007), the cross-sections for γ -ray production (Mori 2009), the optical depth of the 21 cm line of atomic hydrogen (Ackermann et al. 2011), and the relationship of the total molecular column to the measured CO line intensity (Bolatto et al. 2013). In addition to those modeling systematics, the instrumental calibration is only secure at the 10% level (Ackermann et al. 2012). Consequently the γ -ray data can only provide limits on a massive dust component at the level of a few tens of percent of the gas mass.

A complementary approach to this issue is to recognize that the column in condensed H_2 will not be perfectly correlated with the gas column and then to identify the γ -ray emission that is associated specifically with dust—as measured by reddening, say—rather than with the gas. That separation has already been made by Grenier et al. (2005), who inferred a dust-associated mass component at a level $\sim 30\%$ of the measured gas mass. The dust-associated mass was interpreted by Grenier et al. (2005) as dark gas, because the dust itself was assumed to be made up of metals and thus to be a negligible fraction of the mass. But the result could alternatively be interpreted as a large mass contribution in condensed H_2 .

In connection with these two alternative interpretations we note that gas clouds in which hydrogen can condense may have very high central column densities (e.g., $\sim 10^3 \text{ g cm}^{-2}$ for the cloud shown in Figure 3 of Walker & Wardle 2019). So high, in fact, that cosmic-rays cannot penetrate and the γ -ray emissivity is consequently very low—see the calculations in Ohishi et al. (2004). Such clouds are not only “CO dark” but also “ γ -ray dark” and might not be revealed by analyses like that of Grenier et al. (2005).

The γ -ray constraints just described require the condensed H_2 mass to be $\lesssim 60$ times smaller than we estimated in Section 5.5.4—a discrepancy that effectively excludes that particular model. A viable model would require radiative transition rates that are one or two orders of magnitude higher than the $A_{21} \sim 10^{-2} \text{ Hz}$ assumed in Section 5.5.4. That transition rate was based on our calculations for H_2 in the first solvation shell of an ion (Figure 9), so there is little prospect of us reproducing the necessary line strengths within the confines of that particular electrical configuration. For the other electrical configuration that we have studied, that is, the case of a uniform field, the maximum field strength that can

arise from collisional charging of H_2 grains has previously been estimated as $F_{\text{max}} \simeq 1.6 \times 10^{10} \text{ V m}^{-1}$ (Walker 2013), which corresponds to $R_{\text{eq}} \simeq 3.0 \text{ \AA}$ —hence a slightly weaker field than the case shown in Figure 9 and thus similarly unpromising.

Although our models cannot yield the necessary DIB equivalent widths, while simultaneously remaining consistent with the diffuse γ -ray constraints, these are not grounds to reject the possibility of electrified H_2 as a DIB carrier. When compared to the physical circumstances that we are considering, the models we have constructed are highly simplified representations (Section 6.1); more realistic descriptions are needed to address this issue. Although that statement is general, we note in particular that our descriptions of both electrical configurations neglect the fields arising from all of the neighboring, polarized H_2 molecules. Those neighbors introduce substantial high-order multipoles into the electrical potential structure around the molecule of interest, with corresponding contributions to the induced dipole moment (see Equation (8)) and the associated transition rate.

7. Summary and Conclusions

We have investigated the rovibrational eigenstates and ground state rovibrational absorption spectra of H_2 in the $X^1\Sigma_g^+$ electronic ground state, when subjected to an external, static electric field. Our treatment uses recent ab initio calculations of the static electrical response tensors of H_2 , complete up to fourth rank, and substantially improves upon the best previous characterization in the literature. Results were obtained for a pointlike charge $q = \pm e$ at 99 values of the separation R in the range $8 \geq R(\text{\AA}) \geq 2$ and for a uniform field at the same set of field strengths. For each configuration, all transitions stronger than $A_{21} = 10^{-12} \text{ Hz}$, in either parallel or perpendicular polarization, have been tabulated.

In all of the studied configurations, the molecule exhibits absorption lines that are orders of magnitude stronger than any of its field-free rovibrational absorptions from ground state, as a result of the electric dipole moment that is induced by the static field. Consequently, the electrified molecule could feature prominently in astronomical spectra even though it may be only a tiny fraction of the total H_2 column on any line of sight.

The fact that the energy eigenstates of electrified H_2 are mixtures of both rotational and vibrational eigenstates leads to a large number of permitted transitions, so our calculated spectra are much richer than those of the field-free molecule. We find that mixing is much stronger among the vibrationally excited states than for the vibrational ground state, leading to a forest of optical absorption lines for molecules immersed in strong, static fields. These spectra bear little resemblance to the absorption spectra of the field-free molecule, so absent a suitable theoretical template it would be difficult to recognize the carrier as H_2 if any such spectrum appeared in astronomical data.

That point alone is enough to motivate consideration of electrified H_2 as a possible carrier of the DIBs, but we noted two further aspects of our model that reinforce the idea. First, if the electrified molecule were part of a condensed system—as is expected in the interstellar context—then its excited rovibrational states would couple to other vibrational modes of the system, so that rapid internal conversion of the excitation energy would be likely to occur, and this would give the optical absorption lines a diffuse character. Second, we find a rapid increase in the number of transitions as the wavelength

decreases across the near-IR, with only a small number located longward of $\lambda = 1 \mu\text{m}$ —as is known to be the case for the DIBs.

The distribution of transitions with wavelength does, however, also manifest a clear mismatch between the model and the data, with the DIBs observed only down to $\lambda \sim 0.4 \mu\text{m}$, whereas electrified H_2 exhibits a high density of transitions down to at least $\lambda \sim 0.3 \mu\text{m}$.

Considering the variety of microscopic environments that is likely to exist within interstellar condensates, we argued that each transition of electrified H_2 ought to imprint absorption over a band that is very broad indeed—much broader than any of the DIBs. That led us to propose a more specific interpretation: that the DIBs should be identified with points where the transition wavelength is locally stationary with respect to variations in the electrical environment. Because each such point arises from a different microscopic field configuration, the resulting set of absorption peaks will not have tightly correlated equivalent widths, leading to the novel possibility that all of the DIBs might be explicable as absorptions from the ground state of this one carrier.

Despite a huge increase in transition strength relative to the field-free case, the lines of electrified H_2 are still quite weak, and the observed equivalent widths of the DIBs require a large column density in charged H_2 grains, if those grains are indeed the carrier. We estimated their mass contribution to be larger than that of the diffuse gas, but such a large mass in H_2 grains is excluded by the available constraints on unmodeled, diffuse Galactic gamma-ray emission. Because the requisite number of carriers follows fairly directly from the transition strength, which in turn reflects the induced dipole moments, we speculated that this conflict might perhaps be resolved by more realistic descriptions of the electrical environment, accounting for the high-order multipolar fields due to neighboring H_2 molecules—fields that have been entirely neglected in this study. Even so, the transition dipoles would need to be at least an order of magnitude larger than we have calculated in order to be able to explain the DIBs with trace quantities of condensate, and our suggestion of electrified H_2 as the DIB carrier does not sit easily with the current understanding of the ISM.

Among the new transitions that emerge from electrification we found an ortho- H_2 line at very long wavelengths associated with a reorientation of the molecule. Because it is readily thermally excited, even at low temperatures, this transition is potentially important in astrophysical contexts as a cooling line for molecular hydrogen condensates. Observationally it ought to appear as a broad band, reflecting the range of electrical

environments in which the molecules are situated, and we suggested a possible connection to the AME detected from dusty interstellar clouds.

The fact that electrified H_2 has electric dipole transitions at low frequencies—not just the reorientation transition for ortho- H_2 but also the pure rotational lines for both para- and ortho- sequences—means that charged hydrogen dust will emit thermal continuum radiation far more efficiently than any uncharged grains of H_2 . Electrification may be important for both sides of the heating-cooling balance: we noted that thermal far-IR radiation from hydrogen grains can arise from the absorption of starlight in the bands of electrified H_2 , with the rovibrational energy of the latter undergoing internal conversion into phonons. A similar process provides a novel means of exciting suprathreshold mid-IR line emission from H_6^+ , or $(\text{HD})_3^+$, when that ion is surrounded by H_2 ligands.

Although we have made a case that electrified H_2 has astrophysically interesting aspects, that case rests largely on the broad-brush characteristics of our calculated spectra. For example, although we have suggested that electrified H_2 may be a carrier—perhaps even *the* carrier—of the DIBs, we are not in a position to support that proposal with specific predictions for the properties of the individual lines. Moreover, the transition probabilities we estimated are too small to allow trace quantities of electrified H_2 to account for the DIBs, making the proposal incompatible with the accepted picture of the ISM. However, the calculations presented herein are based on a highly simplified representation of the real physical system, which does not accurately describe the strongest electric fields that are of practical interest and does not account at all for either the fields due to neighboring H_2 molecules or the mutual interaction of the electrons in the molecule with those in any adjacent moiety. Quantum chemical treatments are now needed, with a focus on understanding the full spectrum of rovibrational excitations of the H_2 moieties within larger, condensed systems. In parallel, new experimental investigations of the absorption spectra of electrified, condensed H_2 would be valuable—both in the bulk and in the nanocluster form.

Thanks to Bob Brooks for his insights into the laboratory studies of irradiated hydrogens and to Artem Tuntsov for many good discussions about the modeling and a careful reading of the manuscript. I would also like to express my appreciation for some thoughtful refereeing. Access to the Bodleian Library was very helpful, and the author is grateful to the Department of Astrophysics, Oxford, for their hospitality.

Appendix A Graphs of the Electrical Response Tensors of H₂

In this appendix we present, in Figure 10, graphs of the electrical response tensors evaluated by Miliordos & Hunt (2018): 16 independent components, each plotted as a function of the internuclear separation.

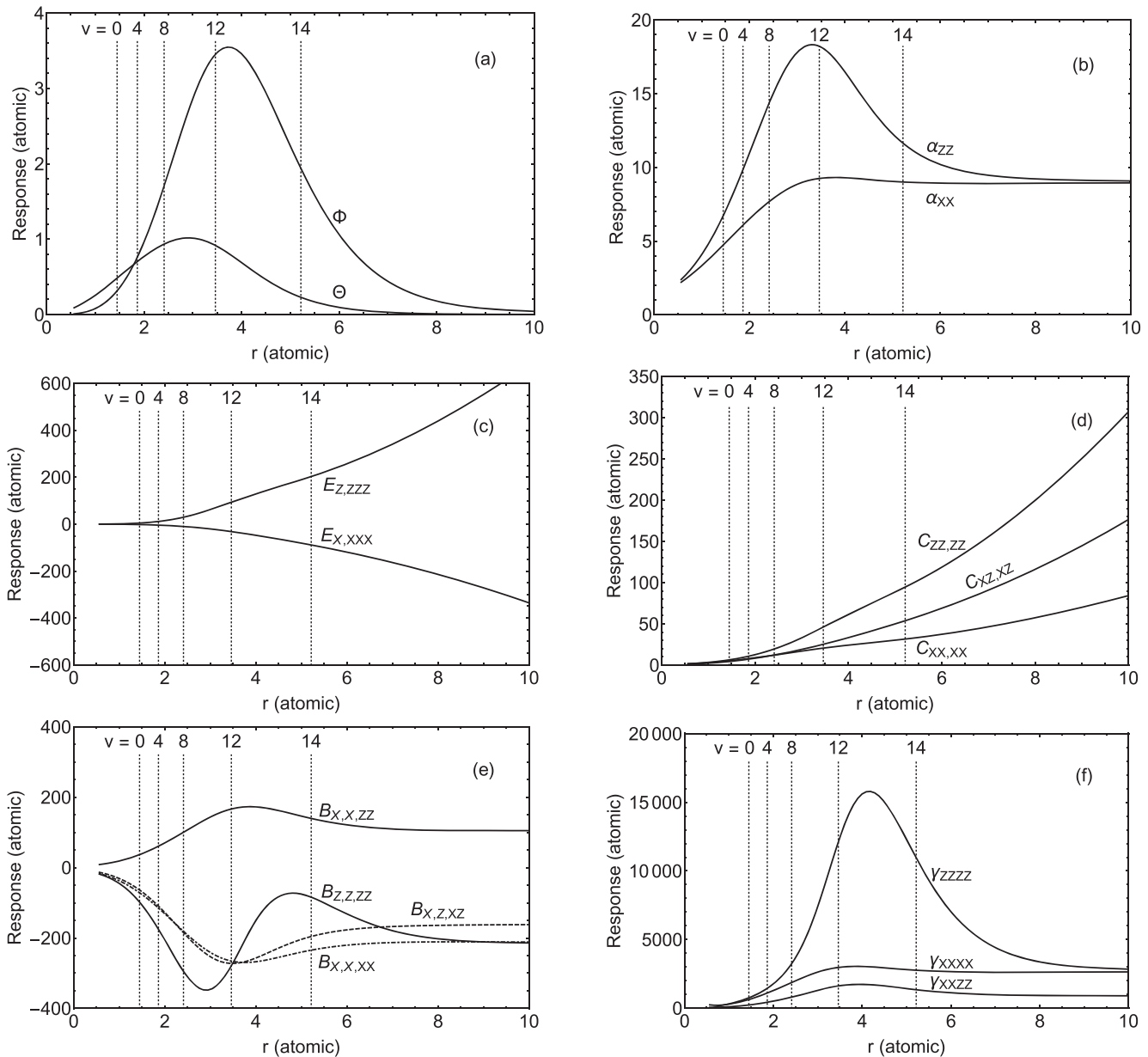


Figure 10. The 16 independent components of the electrical response tensors of H₂, up to fourth rank, evaluated by Miliordos & Hunt (2018) and used in this paper. The Cartesian coordinate system (X, Y, Z) used here is oriented such that the Z -axis is aligned with the internuclear separation vector. Panel (a): the quadrupole $\Theta \equiv \Theta_{zz}$ and the hexadecapole $\Phi \equiv \Phi_{zzzz}$. Panel (b): the dipole polarizability, α . Panel (c): the dipole-octupole polarizability, E . Panel (d): the quadrupole-quadrupole polarizability, C . Panel (e): the dipole-dipole-quadrupole polarizability, B . Panel (f): the second dipole hyperpolarizability, γ . Vertical, dotted lines in each panel show the expected internuclear separations for states with $j = 0$ and vibrational quantum numbers as labeled.

Appendix B Hamiltonian Matrix Elements of the Perturbation

It is convenient to expand the angular structure of the perturbation in spherical harmonics, $Y_{l,n}$. For the electric field configurations considered in this paper, which are both axisymmetric, the only nonzero contributions are from the order $n = 0$. Our description of the electrical response of the molecule extends up to the hexadecapole, so we need only consider degrees $0 \leq l \leq 4$, and the odd terms (dipole, octupole) are guaranteed to be zero because the H_2 molecule is symmetric under inversion through the center of mass. The angular structure of the perturbation is therefore

$$\Delta E(r, \theta, \phi) = a_{0,0}(r)Y_{0,0}(\theta, \phi) + a_{2,0}(r)Y_{2,0}(\theta, \phi) + a_{4,0}(r)Y_{4,0}(\theta, \phi), \quad (\text{B1})$$

where (θ, ϕ) are the polar angles of the internuclear axis of the molecule. The coefficients $a_{0,0}$, $a_{2,0}$, and $a_{4,0}$ are functions of the internuclear separation and depend on the electric field and its first three derivatives—terms up to the hexadecapole, in a multipole expansion of the potential—but are independent of (θ, ϕ) . Integration over the sphere thus allows us to determine the coefficients from

$$a_{l,n} = \int_{4\pi} d\Omega [Y_{l,n}(\theta, \phi)]^* \Delta E, \quad (\text{B2})$$

because the spherical harmonics are orthonormal.

To compute the matrix elements of the Hamiltonian perturbation in the unperturbed Hamiltonian basis, $|v, j, m\rangle$, we first evaluate matrix elements of the spherical harmonics in the angular momentum basis: $\langle j, m | l, n | j', m' \rangle \equiv \langle j, m | Y_{l,n} | j', m' \rangle$. These are almost all zero. In general they can be calculated from

$$\langle j, m | l, n | j', m' \rangle = \left[\frac{(2j+1)(2j'+1)(2l+1)}{4\pi} \right]^{1/2} \frac{1}{(-1)^{m'}} \begin{pmatrix} j & j' & l \\ 0 & 0 & 0 \end{pmatrix} \begin{pmatrix} j & j' & l \\ m & -m' & n \end{pmatrix}, \quad (\text{B3})$$

where the last two factors are Wigner-3J coefficients (which are related to the Clebsch–Gordan coefficients). The nonzero elements lying on or above the leading diagonal are $\langle j, m | 0, 0 | j, m \rangle$, for $j \geq 0$; $\langle j, m | 2, 0 | j, m \rangle$, for $j \geq 1$; $\langle j, m | 2, 0 | j+2, m \rangle$, for $j \geq 0$; $\langle j, m | 4, 0 | j, m \rangle$, for $j \geq 2$; $\langle j, m | 4, 0 | j+2, m \rangle$, for $j \geq 1$; and $\langle j, m | 4, 0 | j+4, m \rangle$, for $j \geq 0$. Those below the leading diagonal can be determined by symmetry.

Although it is straightforward to obtain explicit expressions for these matrix elements in terms of j and m , we do not present those forms here. Instead we recommend that readers use Equation (B3), because functions for rapid evaluation of the Wigner-3J coefficients are readily available in various software packages and programming languages.

B.1. Expansion Coefficients for the Case of a Uniform Field

In the case of a uniform electric field, F , the only contributions to the electrical perturbation come from the dipole polarizability, α , and the second dipole hyperpolarizability, γ . The coefficients in Equation (B1) in this case are

$$a_{0,0} = -\frac{1}{3}\sqrt{\pi}F^2 \left\{ \alpha_{zz} + 2\alpha_{xx} + \frac{1}{60}(3\gamma_{zzzz} + 12\gamma_{xxzz} + 8\gamma_{xxxx})F^2 \right\}, \quad (\text{B4})$$

$$a_{2,0} = -\frac{1}{3}\sqrt{\frac{\pi}{5}}F^2 \left\{ 2\alpha_{zz} - 2\alpha_{xx} + \frac{1}{21}(3\gamma_{zzzz} + 3\gamma_{xxzz} - 4\gamma_{xxxx})F^2 \right\}, \quad (\text{B5})$$

and

$$a_{4,0} = -\frac{2\sqrt{\pi}}{315}(\gamma_{zzzz} - 6\gamma_{xxzz} + \gamma_{xxxx})F^4. \quad (\text{B6})$$

To avoid unnecessary clutter in these expressions, we have not explicitly shown the dependence of the tensor components (α_{zz} , etc.) on the internuclear separation, r .

B.2. Expansion Coefficients for the Case of a Pointlike Elementary Charge

In the field of a pointlike charge none of the derivatives of the electrical potential vanish, so there are contributions to the electrical perturbation associated with all seven response tensors. Let R denote the separation between the charge and the center of mass of the

molecule; then the expansion coefficients in this case are

$$a_{0,0} = -\frac{1}{3}\sqrt{\pi}\frac{q^2}{R^4}\left\{\alpha_{zz} + 2\alpha_{xx} + \frac{3}{5}(C_{zz,zz} + 8C_{xz,xz} + 8C_{xx,xx})\frac{1}{R^2} - \frac{2}{5}(B_{z,z,zz} + B_{x,x,zz} + 4B_{x,z,xz} + 4B_{x,x,xx})\frac{q}{R^3} + \frac{1}{60}(3\gamma_{zzzz} + 12\gamma_{xxxx} + 8\gamma_{xxxx})\frac{q^2}{R^4}\right\}, \quad (\text{B7})$$

$$a_{2,0} = \sqrt{\frac{\pi}{5}}\frac{q}{R^3}\left\{2\Theta - \frac{2}{3}(\alpha_{zz} - \alpha_{xx})\frac{q}{R} - \frac{2}{7}(3E_{z,zzz} - 8E_{x,xxx} + 5C_{zz,zz} + 4C_{xz,xz} - 8C_{xx,xx})\frac{q}{R^3} + \frac{1}{21}(11B_{z,z,zz} + 2B_{x,x,zz} + 8B_{x,z,xz} - 16B_{x,x,xx})\frac{q^2}{R^4} - \frac{1}{63}(3\gamma_{zzzz} + 3\gamma_{xxxx} - 4\gamma_{xxxx})\frac{q^3}{R^5}\right\}, \quad (\text{B8})$$

and

$$a_{4,0} = 2\sqrt{\pi}\frac{q}{R^5}\left\{\frac{1}{3}\Phi - \frac{4}{21}(E_{z,zzz} + 2E_{x,xxx})\frac{q}{R} - \frac{4}{35}(2C_{zz,zz} - 4C_{xz,xz} + C_{xx,xx})\frac{q}{R} + \frac{2}{105}(3B_{z,z,zz} - 2B_{x,x,zz} - 8B_{x,z,xz} + 2B_{x,x,xx})\frac{q^2}{R^2} - \frac{1}{315}(\gamma_{zzzz} - 6\gamma_{xxxx} + \gamma_{xxxx})\frac{q^3}{R^3}\right\}. \quad (\text{B9})$$

Appendix C Transition Dipole Matrix Elements

To determine the transition dipole matrix elements, it is convenient to expand the electric dipole moment operator of the perturbed molecule (8) in spherical harmonics—just as we did for the Hamiltonian of the perturbation in Appendix B. Rather than using the Cartesian form $\mu_\alpha = (\mu_x, \mu_y, \mu_z)$ of the dipole moment, which follows directly from Equation (8), it is simplest to work with the spherical harmonic representation of that vector,

$$\{\mu_{-1}, \mu_0, \mu_{+1}\} = \left\{\frac{1}{\sqrt{2}}(\mu_x - i\mu_y), \mu_z, -\frac{1}{\sqrt{2}}(\mu_x + i\mu_y)\right\}, \quad (\text{C1})$$

and form the spherical harmonic expansion of each of those components. The expressions are given below for the two field configurations studied in this paper.

C.1. Expansion Coefficients for the Case of a Uniform Field

In the case of a uniform electric field, F , the only contributions to the electric dipole come from the dipole polarizability, α , and the second dipole hyperpolarizability, γ . The spherical harmonic expansion coefficients in this case are

$$a_{0,0}(0) = \sqrt{\frac{\pi}{3}}F\left\{2\alpha_{zz} + 4\alpha_{xx} + \frac{1}{15}(3\gamma_{zzzz} + 12\gamma_{xxxx} + 8\gamma_{xxxx})F^2\right\}, \quad (\text{C2})$$

$$a_{2,0}(0) = \frac{4}{3}\sqrt{\frac{\pi}{5}}F\left\{\alpha_{zz} - \alpha_{xx} + \frac{1}{21}(3\gamma_{zzzz} + 3\gamma_{xxxx} - 4\gamma_{xxxx})F^2\right\}, \quad (\text{C3})$$

$$a_{4,0}(0) = \frac{8}{315}\sqrt{\pi}F^3\{\gamma_{zzzz} - 6\gamma_{xxxx} + \gamma_{xxxx}\}, \quad (\text{C4})$$

$$a_{2,1}(1) = a_{2,-1}(-1) = \sqrt{\frac{\pi}{15}}F\left\{2\alpha_{zz} - 2\alpha_{xx} + \frac{1}{21}(3\gamma_{zzzz} + 3\gamma_{xxxx} - 4\gamma_{xxxx})F^2\right\}, \quad (\text{C5})$$

and

$$a_{4,1}(1) = a_{4,-1}(-1) = \frac{2}{63}\sqrt{\frac{2\pi}{5}}F^3\{\gamma_{zzzz} - 6\gamma_{xxxx} + \gamma_{xxxx}\}, \quad (\text{C6})$$

where $a_{l,n}(m)$ denotes the (l, n) coefficient of the spherical harmonic expansion of the μ_m component.

C.2. Expansion Coefficients for the Field of a Pointlike Elementary Charge

In the field of a pointlike charge there are contributions to the dipole induced by the octupole of the applied field and by the dipole-quadrupole of the applied field. The expansion coefficients in this case are

$$a_{0,0}(0) = \frac{1}{3}\sqrt{\pi}\frac{q}{R^2} \left\{ 2\alpha_{zz} + 4\alpha_{xx} - \frac{4}{5}(B_{z,z,zz} + B_{x,x,zz} + 4B_{x,z,xz} + 4B_{x,x,xx})\frac{q}{R^3} \right. \\ \left. + \frac{1}{15}(3\gamma_{zzzz} + 12\gamma_{xxzz} + 8\gamma_{xxxx})\frac{q^2}{R^4} \right\}, \quad (C7)$$

$$a_{2,0}(0) = 2\sqrt{\frac{\pi}{5}}\frac{q}{R^2} \left\{ \frac{2}{3}(\alpha_{zz} - \alpha_{xx}) + \frac{1}{7}(3E_{z,zzz} - 8E_{x,xxx})\frac{1}{R^2} \right. \\ \left. - \frac{1}{21}(11B_{z,z,zz} + 2B_{x,x,zz} + 8B_{x,z,xz} - 16B_{x,x,xx})\frac{q}{R^3} + \frac{2}{63}(3\gamma_{zzzz} + 3\gamma_{xxzz} - 4\gamma_{xxxx})\frac{q^2}{R^4} \right\}, \quad (C8)$$

$$a_{4,0}(0) = \frac{8}{21}\sqrt{\pi}\frac{q}{R^4} \left\{ E_{z,zzz} + 2E_{x,xxx} - \frac{1}{5}(3B_{z,z,zz} - 2B_{x,x,zz} - 8B_{x,z,xz} + 2B_{x,x,xx})\frac{q}{R} \right. \\ \left. + \frac{1}{15}(\gamma_{zzzz} - 6\gamma_{xxzz} + \gamma_{xxxx})\frac{q^2}{R^2} \right\}, \quad (C9)$$

$$a_{2,1}(1) = a_{2,-1}(-1) \\ = \sqrt{\frac{\pi}{15}}\frac{q}{R^2} \left\{ 2\alpha_{zz} - 2\alpha_{xx} - \frac{2}{7}(3E_{z,zzz} - 8E_{x,xxx})\frac{1}{R^2} \right. \\ \left. - \frac{2}{7}(B_{z,z,zz} - 3B_{x,x,zz} + 2B_{x,z,xz} - 4B_{x,x,xx})\frac{q}{R^3} + \frac{1}{21}(3\gamma_{zzzz} + 3\gamma_{xxzz} - 4\gamma_{xxxx})\frac{q^2}{R^4} \right\}, \quad (C10)$$

and

$$a_{4,1}(1) = a_{4,-1}(-1) \\ = \frac{2}{21}\sqrt{\frac{2\pi}{5}}\frac{q}{R^4} \left\{ 5E_{z,zzz} + 10E_{x,xxx} - (3B_{z,z,zz} - 2B_{x,x,zz} - 8B_{x,z,xz} + 2B_{x,x,xx})\frac{q}{R} \right. \\ \left. + \frac{1}{3}(\gamma_{zzzz} - 6\gamma_{xxzz} + \gamma_{xxxx})\frac{q^2}{R^2} \right\}. \quad (C11)$$

ORCID iDs

Mark A. Walker  <https://orcid.org/0000-0002-5603-3982>

References

- Ackermann, M., Ajello, M., Albert, A., et al. 2012, *ApJS*, **203**, 4
 Ackermann, M., Ajello, M., Baldini, L., et al. 2011, *ApJ*, **726**, 81
 Allen, R. J., & Diaz-Miller, R. 2004, in IAU Symp. 220, Dark Matter in Galaxies, ed. S. D. Ryder et al. (San Francisco, CA: ASP), 249
 Atkins, P., & Friedman, R. 2011, *Molecular Quantum Mechanics* (5th ed.; Oxford: Oxford Univ. Press)
 Barbatti, M., Jalbert, G., & Nascimento, M. A. C. 2000, *JChPh*, **113**, 4230
 Barbatti, M., Jalbert, G., & Nascimento, M. A. C. 2001, *JChPh*, **114**, 7066
 Bernstein, L. S., Clark, F. O., & Lynch, D. K. 2013, *ApJ*, **768**, 84
 Bishop, D. M. 1990, *RvMP*, **62**, 343
 Bohr, J. E., & Hunt, K. L. C. 1987, *JChPh*, **86**, 5441
 Bohren, C. F., & Huffman, D. R. 2004, *Absorption and Scattering of Light by Small Particles* (Weinheim: Wiley)
 Bolatto, A. D., Wolfire, M., & Leroy, A. K. 2013, *ARA&A*, **51**, 207
 Brooks, R. L., Bose, S. K., Hunt, J. L., et al. 1985, *PhRvB*, **32**, 2478
 Buckingham, A. D. 1967, in *Advances in Chemical Physics: Intermolecular Forces*, Vol. 12, ed. J. O. Hirschfelder (New York: Wiley), 107
 Calvo, F., & Yurtsever, E. 2018, *JChPh*, **148**, 102305
 Cami, J., & Cox, N. L. J. (ed.) 2014, in IAU Symp. 297, *The Diffuse Interstellar Bands* (Cambridge: Cambridge Univ. Press)
 Cami, J., Sonnentrucker, P., Ehrenfreund, P., & Foing, B. H. 1997, *A&A*, **326**, 822
 Campbell, E. K., Holz, M., Gerlich, D., & Maier, J. P. 2015, *Natur*, **523**, 322
 Chan, M. C., Okumura, M., & Oka, T. 2000, *JPCA*, **104**, 3775
 Clampitt, R., & Gowland, L. 1969, *Natur*, **223**, 815
 Cole, M. W. 1970, *PhRvB*, **2**, 4239
 Condon, E. U. 1932, *PhRv*, **41**, 759
 Cooley, J. W. 1961, *Math. Comput.*, **15**, 363
 Cordiner, M. A., Linnartz, H., Cox, N. L. J., et al. 2019, *ApJL*, **875**, L28
 Cummings, A. C., Stone, E. C., Heikkilä, B. C., et al. 2016, *ApJ*, **831**, 18
 Delahaye, T., Fiasson, A., Pohl, M., & Salati, P. 2011, *A&A*, **531**, A37
 Dickinson, C., Ali-Haïmoud, Y., Barr, A., et al. 2018, *NewAR*, **80**, 1
 Draine, B. T. 2003, *ARA&A*, **41**, 241
 Duley, W. W. 1996, *ApJL*, **471**, L57
 Fajardo, M. E., Lindsay, C. M., & Momose, T. 2009, *JChPh*, **130**, 244508
 Field, G. B. 1969, *MNRAS*, **144**, 411
 Foing, B. H., & Ehrenfreund, P. 1994, *Natur*, **369**, 296
 Freiman, Y. A., & Crespo, Y. 2017, *LTP*, **43**, 1345
 Friedman, S. D., York, D. G., McCall, B. J., et al. 2011, *ApJ*, **727**, 33
 Füglistaler, A., & Pfenniger, D. 2018, *A&A*, **613**, A64
 Geballe, T. R., Najjarro, F., Figer, D. F., Schlegelmilch, B. W., & de la Fuente, D. 2011, *Natur*, **479**, 200
 Gerhard, O., & Silk, J. 1996, *ApJ*, **472**, 34
 Greenberg, J. M., & de Jong, T. 1969, *Natur*, **224**, 251
 Grenier, I. A., Casandjian, J.-M., & Terrier, R. 2005, *Sci*, **307**, 1292
 Hensley, B. S., Draine, B. T., & Meisner, A. M. 2016, *ApJ*, **827**, 45
 Herbig, G. H. 1995, *ARA&A*, **33**, 19
 Herzberg, G. 1950, *Molecular Spectra and Molecular Structure. Vol. I—Spectra of Diatomic Molecules* (Malabar: Krieger)
 Hobbs, L. M., York, D. G., Snow, T. P., et al. 2008, *ApJ*, **680**, 1256
 Hobbs, L. M., York, D. G., Thorburn, J. A., et al. 2009, *ApJ*, **705**, 32
 Huang, L., Matta, C. F., & Massa, L. 2011, *JPCA*, **115**, 12445
 Hunter, S. D., Bertsch, D. L., Catelli, J. R., et al. 1997, *ApJ*, **481**, 205

- Jaksch, S., Mauracher, A., Bacher, A., et al. 2008, *JChPh*, **129**, 224306
- Jenniskens, P., & Désert, F. X. 1994, *A&AS*, **106**, 39
- Joblin, C., Maillard, J. P., d'Hendecourt, L., & Léger, A. 1990, *Natur*, **346**, 729
- Johnson, B. R. 1977, *JChPh*, **67**, 4086
- Kerr, T. H., Hibbens, R. E., Miles, J. R., et al. 1996, *MNRAS*, **283**, L105
- Kettwich, S. C., Anderson, D. T., Walker, M. A., & Tuntsov, A. V. 2015, *MNRAS*, **450**, 1032
- Kolos, W., & Wolniewicz, L. 1967, *JChPh*, **46**, 1426
- Komasa, J., Piszczatowski, K., Lach, G., et al. 2011, *J. Chem. Theory Comput.*, **7**, 3105
- Komasa, J., Puchalski, M., Czachorowski, P., Lach, G., & Pachucki, K. 2019, *PhRvA*, **100**, 032519
- Kraushaar, W. L., Clark, G. W., Garmire, G. P., et al. 1972, *ApJ*, **177**, 341
- Kumada, T., Tachikawa, H., & Takayanagi, T. 2005, *PCCP*, **7**, 776
- Kurosaki, Y., & Takayanagi, T. 1998, *JChPh*, **109**, 4327
- Lan, T.-W., Ménard, B., & Zhu, G. 2015, *MNRAS*, **452**, 3629
- Levine, W. G., & Laughlin, G. 2021, *ApJ*, **912**, 3
- Libbrecht, K. G. 2017, *AnRMS*, **47**, 271
- Lin, C. Y., Gilbert, A. T. B., & Walker, M. A. 2011, *ApJ*, **736**, 91
- McCall, B. J., Drosback, M. M., Thorburn, J. A., et al. 2010, *ApJ*, **708**, 1628
- McLean, A. D., & Yoshimine, M. 1967, *JChPh*, **47**, 1927
- Mengel, M., Winnewisser, B. P., & Winnewisser, M. 1998, *JMoSp*, **188**, 221
- Miliordos, E., & Hunt, K. L. C. 2018, *JChPh*, **149**, 234103
- Miller, S. M., Tennyson, J., Geballe, T. R., & Stallard, T. 2020, *RvMP*, **92**, 035003
- Mohammadi, A., Nasiri, S., & Zahedi, M. 2020, *CPL*, **744**, 137216
- Momose, T., Lindsay, C. M., Zhang, Y., & Oka, T. 2001, *PhRvL*, **86**, 4795
- Mori, M. 2009, *Aph*, **31**, 341
- Ohishi, M., Mori, M., & Walker, M. A. 2004, *ApJ*, **610**, 868
- Pachucki, K. 2010, *PhRvA*, **82**, 032509
- Pachucki, K., & Komasa, J. 2011, *PhRvA*, **83**, 032501
- Pachucki, K., & Komasa, J. 2014, *JChPh*, **141**, 224103
- Pfenniger, D., & Combes, F. 1994, *A&A*, **285**, 94
- Pfenniger, D., Combes, F., & Martinet, L. 1994, *A&A*, **285**, 79
- Pipin, J., & Bishop, D. M. 1992, *JPhB*, **25**, 17
- Planck Collaboration, Abergel, A., Ade, P. A. R., et al. 2014, *A&A*, **566**, A55
- Poll, J. D., & Hunt, J. L. 1985, *CaJPh*, **63**, 84
- Poll, J. D., & Wolniewicz, L. 1978, *JChPh*, **68**, 3053
- Renzler, M., Kuhn, M., Mauracher, A., et al. 2016, *PhRvL*, **117**, 273001
- Rouef, E., Abgrall, H., Czachorowski, P., et al. 2019, *A&A*, **630**, A58
- Ryder, S. D., Pisano, D. J., Walker, M. A., & Freeman, K. C. (ed.) 2004, IAU Symp. 220, Dark Matter in Galaxies (San Francisco, CA: ASP)
- Sandford, S. A., & Allamandola, L. J. 1993, *ApJL*, **409**, L65
- Sarre, P. J. 2006, *JMoSp*, **238**, 1
- Sarre, P. J., Miles, J. R., Kerr, T. H., et al. 1995, *MNRAS*, **277**, L41
- Seab, C. G., & Snow, T. P. 1985, *ApJ*, **295**, 485
- Seligman, D., & Laughlin, G. 2020, *ApJL*, **896**, L8
- Silvera, I. F., & Goldman, V. V. 1978, *JChPh*, **69**, 4209
- Snow, T. P. 1995, *CPL*, **245**, 639
- Snow, T. P. 2004, in ASP Conf. Ser. 309, Astrophysics of Dust, ed. A. N. Witt, G. C. Clayton, & B. T. Draine (San Francisco, CA: ASP), **93**
- Snow, T. P., York, D. G., & Resnick, M. 1977, *PASP*, **89**, 758
- Sorokin, P. P., & Glowina, J. H. 1995, *CPL*, **234**, 1
- Sorokin, P. P., & Glowina, J. H. 1996, *ApJ*, **473**, 900
- Souers, P. C., Fearon, E. M., Roberts, P. E., et al. 1980, *PhL*, **77A**, 277
- Strong, A. W., Moskalenko, I. V., & Ptuskin, V. S. 2007, *ARNPS*, **57**, 285
- Swaters, R. A., Sancisi, R., van der Hulst, J. M., & van Albada, T. S. 2012, *MNRAS*, **425**, 2299
- Turner, J., Kirby-Docken, K., & Dalgarno, A. 1977, *ApJS*, **35**, 281
- van de Hulst, H. C. 1981, Light Scattering by Small Particles (New York: Dover)
- Walker, M. A. 2013, *MNRAS*, **434**, 2814
- Walker, M. A., & Wardle, M. J. 2019, *ApJ*, **881**, 69
- Wang, X., & Andrews, L. 2004, *JPCA*, **108**, 1103
- White, R. S. 1996, *ApSS*, **240**, 75
- Whittet, D. C. B. 2004, in ASP Conf. Ser. 309, Astrophysics of Dust, ed. A. N. Witt, G. C. Clayton, & B. T. Draine (San Francisco, CA: ASP), **65**